

Quantum phase transition and composite excitations of antiferromagnetic quantum spin trimer chains in a magnetic field

Jun-Qing Cheng,^{1,2} Zhi-Yao Ning,¹ Han-Qing Wu,^{1,*} and Dao-Xin Yao^{1,†}

¹*State Key Laboratory of Optoelectronic Materials and Technologies, Center for Neutron Science and Technology, Guangdong Provincial Key Laboratory of Magnetoelectric Physics and Devices, School of Physics, Sun Yat-Sen University, Guangzhou 510275, China*

²*School of Physical Sciences, Great Bay University, 523000, Dongguan, China, and Great Bay Institute for Advanced Study, Dongguan 523000, China*

(Dated: June 7, 2024)

Motivated by recent advancements in theoretical and experimental studies on the high-energy excitations, we theoretically explore the quantum phase transition and composite dynamics of the antiferromagnetic trimer chains in a magnetic field using the exact diagonalization, density matrix renormalization group, time-dependent variational principle and cluster perturbation theory. We measure the entanglement entropy to uncover the phase diagram, encompassing the XY-I, 1/3 magnetization plateau, XY-II and ferromagnetic phases. Both critical XY-I and XY-II phases are both described by the conformal field theory with the central charge $c \simeq 1$. By analyzing the dynamical structure factor, we elucidate the distinct features of spin dynamics across different phases. In the regime of weak intertrimer interaction, we identify the intermediate-energy and high-energy modes in the XY-I and 1/3 magnetization plateau phases as the internal trimer excitations, corresponding to the propagation of doublon and quarton, respectively. Notably, the application of a magnetic field splits the high-energy spectra into two branches labeled as the upper quarton and lower quarton. Furthermore, we also explore the spin dynamics of a trimerized model closely related to the quantum magnet $\text{Na}_2\text{Cu}_3\text{Ge}_4\text{O}_{12}$, and discuss the possibility of the quarton Bose-Einstein condensation. Our results can be verified in the inelastic neutron scattering experiments and provide deep insights for exploring the high-energy exotic excitations.

I. INTRODUCTION

Understanding the profound physical nature in the strongly correlated many-body systems is a challenging and fascinate task in modern condensed-matter physics. The interplay of strong quantum fluctuations and interactions gives rise to a variety of exotic phenomena, which have attracted significant interest in the study of low-dimensional correlated systems. Particularly, quasi one-dimensional (1D) magnetic materials derived from the physics of the Heisenberg antiferromagnetic chain (HAC) and its extensions have been extensively investigated [1]. The dynamical behavior, characterized by the spin excitation, play a crucial role in understanding the magnetic structure of quantum materials, and can be studied both theoretically and experimentally [2–14]. Notably, the gapless two-spinon continuum [2] has been observed through inelastic neutron scattering in quasi 1D material KCuF_3 [3, 4] and the frustrated ferromagnetic spin-1/2 chain compound LiCuVO_4 [5]. The multi-spin excitations can be detected using the resonant inelastic X-ray scattering (RIXS) technique [6, 7] in the HAC material Sr_2CuO_3 . Furthermore, the high-energy string excitations have been proposed as the dominant excitations in the isotropic Heisenberg antiferromagnet based on the Bethe ansatz [8], and recently been observed in the antiferromagnetic Heisenberg–Ising chain compounds

$\text{SrCo}_2\text{V}_2\text{O}_8$ and $\text{BaCo}_2\text{V}_2\text{O}_8$ under strong longitudinal magnetic fields using the high-resolution terahertz spectroscopy [9, 10].

Besides the uniform spin chains, quantum materials often exhibit structures consisting of more than one spin per unit cell, resulting in a wider range of magnetic properties. Ladder systems are well studied examples of 1D systems with unit cells, where the gapless or gapped excitation spectrum depend on the rungs consisting of an odd or even number of $S = 1/2$ spins, respectively [15]. This behavior is similar to the Haldane’s conjecture on spin chains with half-odd-integer or integer spins [16]. Among the experimental realizations, the two-leg ladder compound $(\text{C}_7\text{H}_{10}\text{N})_2\text{CuBr}_4$ is noteworthy due to the excellent agreement between its experimental results and the dynamic spin structure factor from the model calculations [17]. The unit cells can effectively form linear chains, with different behaviors observed for systems with an even or odd number of spins in each cell. For example, the model with two-spin unit cells, with repeated couplings $J_1 - J_2$, is well studied. A gap is present in the spectrum if $J_1 \neq J_2$, as the modulation leads to the spinons of the uniform the HAC ($J_1 = J_2$) confining into “triplons” that can be regarded as weakly bound spinon pairs if $J_2 \approx J_1$ [18]. However, the model with three-spin unit cells, with repeated couplings $J_1 - J_1 - J_2$, has a gapless two-spinon continuum [11]. Furthermore, the three-spin unit cells can also be coupled to each other in many other ways, as seen in the trimer chains like $\text{A}_3\text{Cu}_3(\text{PO}_4)_4$ ($\text{A} = \text{Ca}, \text{Sr}, \text{Pb}$) [19–24] and $(\text{C}_5\text{H}_{11}\text{NO}_2)_2 \cdot 3 \text{CuCl}_2 \cdot 2 \text{H}_2\text{O}$ [25], where two spins

* wuhanq3@mail.sysu.edu.cn

† yaodaax@mail.sysu.edu.cn

in one trimer are coupled to two spins of their neighboring trimers. This is in contrast to the ladders, where all spins in a rung are uniformly coupled to spins in neighboring rungs. In the iridate $\text{Ba}_4\text{Ir}_3\text{O}_{10}$, where three-spin unit cells form the layered trimers, the anomalous fractional spinons have been observed in the RIXS experiment [26, 27].

Recently, we have conducted an investigation into the spin dynamics of a trimer chain with repeated couplings $J_1 - J_1 - J_2$ (intratrimer $J_1 \geq$ intertrimer J_2), and found that its low-energy effective model is the uniform HAC with spin $S = 1/2$ in each trimer [11]. The low-energy excitations are still the gapless spinons in the reduced Brillouin zone, particularly for $J_2/J_1 < 1$. When $J_2 = J_1$, the trimer chain reduces to the conventional HAC with the two-spinon continuum, indicating that the low-energy spinons reside in different Brillouin zones. Most interestingly, the composite excitations of the novel quasiparticles, doublons and quartons have been predicted at the intermediate-energy and high-energy spectra, respectively, and immediately confirmed in the inelastic neutron scattering measurements on $\text{Na}_2\text{Cu}_3\text{Ge}_4\text{O}_{12}$ [12]. As $J_2/J_1 \rightarrow 1$, the doublons and quartons lose their identity and fractionalize into the standard two-spinon continuum. The high-energy spin excitations exhibit intriguing physical properties, but remain insufficiently explored. Previous studies have investigated the high-energy excitations in the antiferromagnetic parent compounds of the high-Tc superconductors [28–32], and other systems described by the 2D Heisenberg models [33–36]. It is crucial to delve deeper into these high-energy physics that beyond the spin waves, such as the doublons, quartons and string excitations.

From a theoretical perspective, it is interesting to examine the influence of a magnetic field on the doublons and quartons in the trimer chain illustrated in Fig. 1(a). In this work, we employ various techniques including the exact diagonalization (ED), density matrix renormalization group (DMRG) [37–39], time-dependent variational principle (TDVP) [40, 41], and cluster perturbation theory (CPT) [42–45] to investigate the excitation spectra of trimer chain under the magnetic field. Firstly, we obtain the phase diagram of ground state using the DMRG method. By mapping the entanglement entropy onto the parameter space, we identify the XY-I, 1/3 magnetization plateau, XY-II and ferromagnetic phases. In the gapless XY-I and XY-II phases, both the central charges $c \simeq 1$ indicate that these two phases are well described by the conformal field theory. Additionally, we study the intermediate-energy and high-energy excitations for small g in the XY-I and 1/3 magnetization plateau phases. Our analysis demonstrates that the intermediate-energy and high-energy modes are primarily governed by the internal trimer excitations, referred to as the doublons and quartons, respectively. Furthermore, these features of excitation spectra can also be observed in the spin chain with trimer structure that is closely associated with the quantum magnet $\text{Na}_2\text{Cu}_3\text{Ge}_4\text{O}_{12}$ [12].

The magnetic field drives the lower quarton to approach zero energy, thereby suggesting the potential for the observation of the magnetic-field-induced quarton Bose-Einstein condensation (BEC) in the quantum magnet $\text{Na}_2\text{Cu}_3\text{Ge}_4\text{O}_{12}$. Our results may facilitate further exploration of the high-energy spin excitation mechanisms in other systems containing clusters with odd spins.

II. RESULTS

A. Model

The Hamiltonian of the spin-1/2 antiferromagnetic trimer chain in the presence of a longitudinal magnetic field with periodic boundary conditions reads

$$\mathcal{H} = \sum_{i=1}^N [J_1 (\mathbf{S}_{i,a} \cdot \mathbf{S}_{i,b} + \mathbf{S}_{i,b} \cdot \mathbf{S}_{i,c}) + J_2 \mathbf{S}_{i,c} \cdot \mathbf{S}_{i+1,a}] - H_z \sum_{j=1}^{3N} S_j^z, \quad (1)$$

where $\mathbf{S}_{i,\gamma}$ is the spin-1/2 operator at the γ -th site in the i -th trimer, the intratrimer labels $\gamma \in \{a, b, c\}$ are explained by Fig. 1(a). H_z represents the strength of external magnetic field, which breaks the $\text{SU}(2)$ symmetry. The system consists of a total of N trimers, resulting in a system length of $L = 3N$. The tuning parameter g is defined as $g = J_2/J_1$. For simplicity, we set the intratrimer interaction $J_1 = 1$ as the energy unit, so that intertrimer interaction $J_2 = g$. Our interest is in the range of coupling ratios $g \in [0, 1]$, where the system evolves between the isolated trimers and the isotropic HAC.

B. Quantum phase transition

In the absence of a magnetic field, the antiferromagnetic quantum spin trimer chain exhibits a gapless low-energy excitation known as the two-spinon continuum [11]. When a magnetic field is applied, the $\text{SU}(2)$ symmetry is broken, leading to the emergence of a quantum phase transition driven by the competition between the interaction and magnetic field. In this subsection, we aim to investigate the detailed phase diagram using the DMRG method.

Quantum entanglement provides a unique perspective for unveiling the ground state properties of a many-body system, and has been widely employed to study the quantum phase transitions [46–51]. Entanglement entropy, as a fundamental measurement of bipartite quantum entanglement, can be readily obtained through DMRG calculations. Its definition is given by

$$S = -\text{Tr} [\rho_A \ln \rho_A], \quad (2)$$

where the reduced density matrix ρ_A is the partial trace of the density matrix ρ of whole system $\rho_A = \text{Tr}_B [\rho]$. If

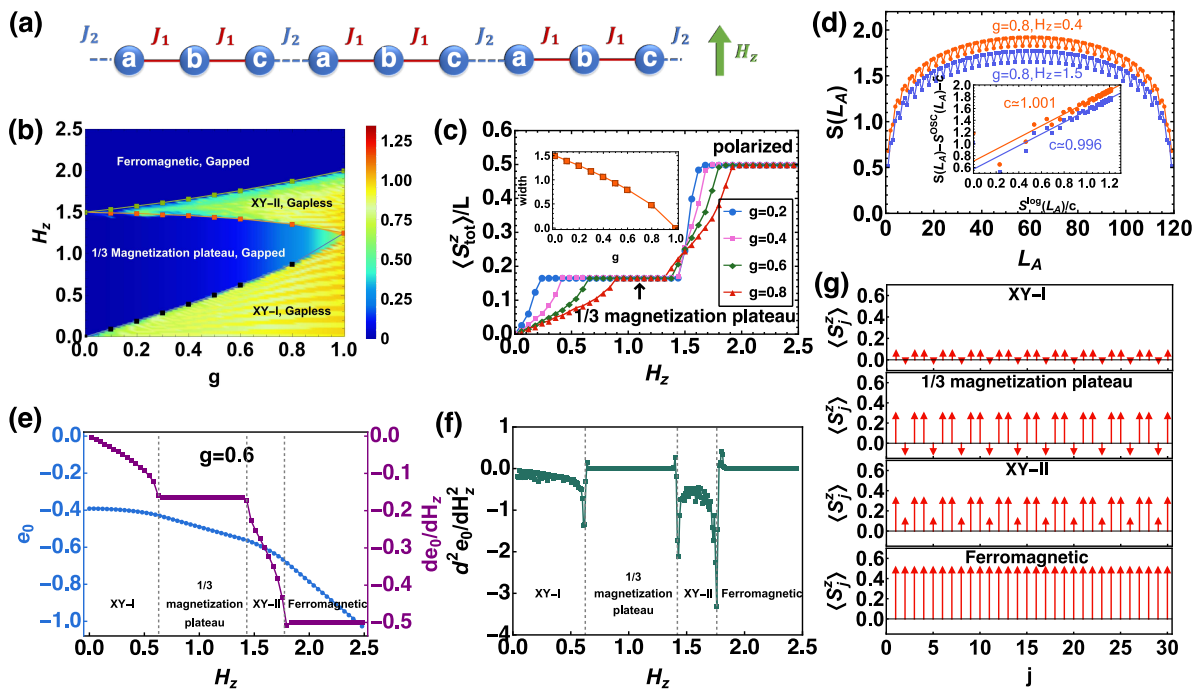


FIG. 1. **Quantum phase transitions.** (a) Schematic representation of a trimer spin chain under a longitudinal magnetic field. We here consider systems with $J_1 \geq J_2 > 0$, and use the letters a, b, c as indicated to refer to the three spins within a unit cell. (b) Phase diagram obtained by employing the DMRG to map the entanglement entropy onto the parameter space (g, H_z) for a system with $L = 180$ spins. (c) Magnetization curves as a function of H_z for different g . Inset shows the width of 1/3 magnetization plateau as function of g . (d) Entanglement entropy $S(L_A)$ as a function of the subsystem size L_A with open boundary conditions. Solid lines of inset are best fits to the CFT scaling form. The best-fit values for the central charges are given. (e) Ground state energy of per spin $e_0 = E_0/L$ and its first derivative de_0/dH_z as a function of H_z for the system with $L = 210$. (f) The second derivative d^2e_0/dH_z^2 as a function of H_z for the system with $L = 210$. (g) Magnetization of every spin obtained by DMRG for four phases where $g = 0.6$ and $H_z = 0.3, 1.0, 1.5, 2.0$.

A and B are entangled, the reduced density matrix must be a mixed state and the entanglement entropy quantifies this degree of mixing. By effectively analyzing the entanglement entropy, the characteristics of ground states in various quantum phases can be extracted. Therefore, the entanglement entropy serves as a viable and useful tool for investigating the quantum phase transitions. As illustrated in Fig. 1(b), the entanglement entropy reveals four distinct phases in the (g, H_z) parameter space. Applying an external magnetic field, a Néel to incommensurate phase transition occurs, leading the system into the XY-I Phase. However, the magnetic field is not strong enough to open a gap, thus the ground state is still gapless with a nonzero entanglement entropy. In Fig. 1(c), the magnetization grows with the increase of magnetic field in this XY-I phase until a fractional magnetization plateau is present.

The fractional magnetization plateau in the magnetization curves can be understood through the Oshikawa-Yamanaka-Affleck (OYA) criterion [52]:

$$n(s - m) = \text{integer} \quad (3)$$

where n is the number of spin in a unit cell, m is the magnetization per site in unit and s denotes the magnitude of spin. In the trimer chain, it has $n = 3$, $s = 1/2$,

so when $n(s - m) = 0$ it has $m = 1/2$ corresponding to the total polarized case, and when $n(s - m) = 1$ it has $m = 1/6$ corresponding to the 1/3 magnetization plateau. Fig. 1(c) clearly illustrates the presence of these two plateaus. In the 1/3 magnetization plateau phase, the external magnetic field is not strong enough to decouple the singlets. As g increases, the width of magnetization plateau decreases, eventually disappearing at $g = 1$ where the trimer chain becomes the uniform Heisenberg chain. From the magnetization of each spin, as shown in Fig. 1(g), we can observe that the magnetization follows a periodic pattern in terms of the trimerized structure. Specifically, the magnetization of central spin of each trimer flips up as H_z increases. Importantly, the magnetization of each spin remains fixed even as the magnetic field increases in the 1/3 magnetization plateau phase. The ground state of an isolated trimer in the presence of magnetic field is given by,

$$|0\rangle = \frac{1}{\sqrt{6}} (|\uparrow\uparrow\downarrow\rangle - 2|\uparrow\downarrow\uparrow\rangle + |\downarrow\uparrow\uparrow\rangle), \quad (4)$$

which is also the antiferromagnetic trimer state of the Haldane plateau in one-dimensional $(S, s) = (1, 1/2)$ mixed spin chain where the spin $S = 1$ is represented by

two spins $S = 1/2$ [53]. In the $1/3$ magnetization plateau phase, as shown in Fig. 1(g), the expectation values of the z component of three spins a, b, c are 0.322 , -0.144 , and 0.322 , respectively, which are approximately coincide with the ideal state with expectation values $1/3$, $-1/6$, and $1/3$. It indicates that the $1/3$ magnetization plateau state exhibits the Néel order along the magnetic field, with each trimer having an effective spin $1/2$, giving the appearance of polarization for each trimer.

As the magnetic field increases, the singlets are destroyed, leading to the presence of the XY-II phase. The system remains gapless with a nonzero entanglement entropy in ground state, and the average of magnetization is larger than the one in XY-I phase, and also increases with the magnetic field. As long as the magnetic field is strong enough, all spins become polarized, resulting in the formation of the other magnetization plateau and the presence of ferromagnetic phase. We also use entanglement properties to indicate the possible conformal field theory description of the gapless phases. The Rényi entanglement entropy of subsystem A is given by

$$S_\nu(\rho_A) = \frac{1}{1-\nu} \ln(\text{Tr}\{\rho_A^\nu\}). \quad (5)$$

In the limit $\nu \rightarrow 1$, the above expression reduces to the von Neumann entanglement entropy,

$$S(\rho_A) = \lim_{\nu \rightarrow 1} S_\nu(\rho_A) = -\text{Tr}[\rho_A \ln \rho_A]. \quad (6)$$

The Rényi entanglement entropy of subsystem A follows the scaling form [54–56]:

$$S_\nu(L_A) = S_\nu^{\text{log}}(L_A) + S_\nu^{\text{osc}}(L_A) + \tilde{c}_\nu, \quad (7)$$

where

$$S_\nu^{\text{log}}(L_A) = \frac{c}{6\eta} \left(1 + \frac{1}{\nu}\right) \ln \left\{ \left[\frac{\eta L}{\pi} \sin \left(\frac{\pi L_A}{L} \right) \right] \right\}, \quad (8)$$

and

$$S_\nu^{\text{osc}}(L_A) = F_\nu \left(\frac{L_A}{L} \right) \frac{\cos(2k_F L_A)}{\left| \frac{2\eta L}{\pi} \sin(\pi L_A/L) \right|^{\frac{2\Delta_1}{\nu}}}. \quad (9)$$

Here, $\eta = 1, 2$ is for periodic and open boundary conditions, respectively. The central charge c , the Fermi momentum k_F , and the scaling dimension Δ_1 are universal parameters. $F_\nu(L_A/L)$ is a universal scaling function and \tilde{c} is a nonuniversal constant. By fitting the DMRG data with these functions for $\nu = 1$, we extract the central charges of two XY phases as indicators of their universality classes. As shown in Fig. 1(c), the two XY phases are both described by the conformal field theory with the central charges $c \simeq 1$.

Furthermore, in order to identify the types of quantum phases transitions present, we have conducted an analysis involving the computation of the first and second derivatives of the ground state energy with respect to

the magnetic field H_z , see Figs. 1(e) and 1(f). According to the Hellmann-Feynman theorem, the magnetization curves (see Fig.1(c)) and the first derivative of ground state energy de_0/dH_z reveal the similar behaviors, characterized by continuity but lack of differentiability near the critical points. The second derivative d^2e_0/dH_z^2 exhibits nonanalytic behaviors in the vicinity of the critical points. These results collectively suggest that the quantum phase transitions between XY-I, $1/3$ magnetization plateau, XY-II and ferromagnetic phases are the second-order quantum phase transitions. In Supplementary note 1, we also provide the real-space spin-spin correlation function for four phases. The correlation functions in XY-I and XY-II phases decay according to power laws with the critical exponents converging towards 1, which is similar to the $S = 1/2$ isotropic Heisenberg chain [57].

C. Excitation spectra

In this section, we present the spin excitation spectra of the trimer chain in an external magnetic field using the dynamical structure factor (DSF):

$$\mathcal{S}^{\alpha\beta}(q, \omega) = \sum_j e^{-iqj} \left[\int_{-\infty}^{\infty} dt e^{i\omega t} \langle \hat{S}_j^\alpha(t) \hat{S}_0^\beta \rangle \right], \quad (10)$$

where α, β refer to the spin components x, y , and z . We calculated the DSF using the CPT and DMRG-TDVP methods to study the spin dynamics under the modification of control parameters, g and H_z . The calculation details can be found in the Sec. V. In our previous study, we have utilized the quantum Monte Carlo with subsequent numerical analytic continuation to investigate the spin dynamics of trimer chain in absent of magnetic field, and revealed the doublons and quartons in the intermediate-energy and high-energy regimes, respectively [11]. As a comparison, the spectral characteristics are also assessed using the DMRG-TDVP and CPT calculations, the results can be found in Supplementary note 2. Furthermore, we provide the spin excitation spectra obtained by the ED calculation in Supplementary note 5.

In Fig. 2, the transverse excitation spectra $\mathcal{S}^{xx}(q, \omega)$ for four phases are present. The excitations are gapless in two XY phases and gapped in the $1/3$ magnetic plateau and ferromagnetic phases. To understand the spin dynamics of XY-I and XY-II phases, let us examine the zero-energy excitations. The incommensurability appearing in the spin dynamics for an AF spin-1/2 chain under a longitudinal magnetic field can be understood in terms of spinless fermion language [58]. The longitudinal magnetic field is equivalent to a chemical potential, which modifies the filling of the band and splits the degeneracy of the electron-hole bands. The intraband and interband zero-energy excitations correspond to the longitudinal and transverse fluctuations, respectively. For the trimer chain with a longitudinal magnetic field, the incommensurability arises from the splitting of

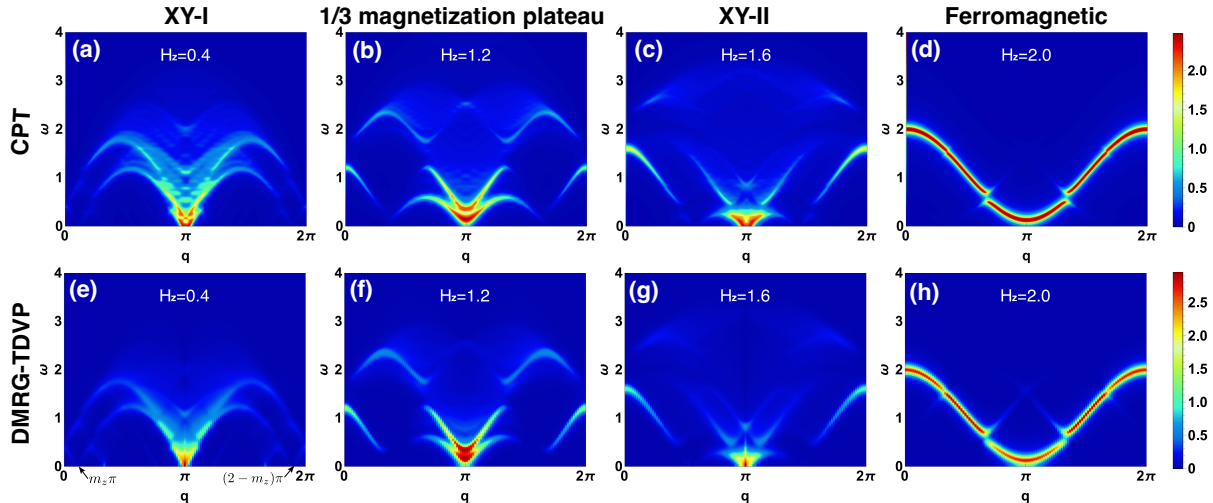


FIG. 2. $S^{xx}(q, \omega)$ obtained from CPT and DMRG-TDVP calculations for different phases. $S^{xx}(q, \omega)$ in (a)(e) XY-I phase, (b)(f) 1/3 magnetization plateau phase, (c)(g) XY-II phase, and (d)(h) Ferromagnetic phase. All results are from the case where $g = 0.8$, and the DMRG-TDVP calculations are from the length $L = 120$. The color coding of $S^{xx}(q, \omega)$ uses a piecewise function with the boundary value $U_0 = 2$. Below the boundary, the low-intensity portion is characterized by a linear mapping of the spectral function to the color bar, while above the boundary a logarithmic scale is used, $U = U_0 + \log_{10}[S^{zz}(q, \omega)] - \log_{10}(U_0)$.

the bands. Figs. 2(a)(e) display the transverse excitations $S^{xx}(q, \omega)$ changing the number of particles, which give rise to fluctuations reach the zero energy at incommensurate wave numbers $q = m_z\pi$ and $q = (2 - m_z)\pi$ in addition to $q = \pi$. The spectral weight is concentrated at the commensurate positions corresponding to each reciprocal lattice points of $q = \pi$ in the XY-I and XY-II phases. At the high-energy regime, the continuum is observed both in the 1/3 magnetization plateau and XY-II phases. At the ferromagnetic phase, see Figs. 2(d)(h), all spins are polarized, the spin excitation is still the propagation of magnon. Some energy gaps are observed at the Brillouin zone edges $q = \pi/3, 2\pi/3, 4\pi/3, 5\pi/3$ where the spin waves are diffracted due to the periodic potential of the trimerized interaction, therefore the magnons at the Brillouin zone edges have two energies for the same wave vector. In Supplementary note 3, we also present the longitudinal excitation spectrum and discuss the zero-energy excitations corresponding to the longitudinal fluctuations.

In our previous study [11], we have found that the smaller g induces rich intermediate-energy and high-energy excitations beyond the spin wave. Therefore, it is of great interest to investigate the evolutions of intermediate-energy and high-energy quasiparticles referred to as the doublons and quartons under the magnetic field. Next, we focus on the weak intertrimer coupling $g = 0.3$ to study their dynamical evolutions. In this case, the system is nearly isolated trimer, and can be analyzed simply. From Figs. 3(a)(e), we observe that the low-energy excitation is similar to the excitation spectrum of conventional spinon under the magnetic field, a split of the dispersion relation occurs, which is characterized by the emergent fermions of Heisenberg chain in the

magnetic field [59]. The intermediate-energy spectrum has little separation near $q = \pi/3$ and $q = 5\pi/3$, and a continuum emerges possibly due to the propagation of doublons dressed by spinons [11]. The high-energy spectrum is clearly split into two branches by the magnetic field.

As H_z increases, see Figs. 3(b)(f), the excitation gap opens, leading the system into a 1/3 magnetization plateau phase. Consequently, the lower spectrum of high-energy excitations with $\Delta M = -1$ transitions to the low-energy regime. When $H_z = 1.5$, the system progresses into the gapless XY-II phase (see Figs. 3(c)(g)), where the low-energy, intermediate-energy and high-energy spectra exhibit clear differentiation. At the ferromagnetic phase $H_z = 2.0$, shown in Figs. 3(d)(h), the spin excitation remains dominated by spin waves due to full spin polarization. Some energy gaps are also observed at the Brillouin zone edges $q = \pi/3, 2\pi/3, 4\pi/3, 5\pi/3$, which is consistent with the results of Figs. 2(d)(h).

The preceding discourse primarily centers on the impact of a magnetic field on the spin excitation spectra of a trimer chain with a constant intertrimer interaction strength. In order to deepen our comprehension of the spin dynamics within such a trimer chain in the presence of a magnetic field, we present additional results obtained through DMRG-TDVP calculations for varying values of the g parameter. Details are provided in Supplementary Note 4 for further elucidation.

D. Excitations mechanisms

In order to gain a deeper understanding of the intermediate-energy and high-energy spin dynamics, it is

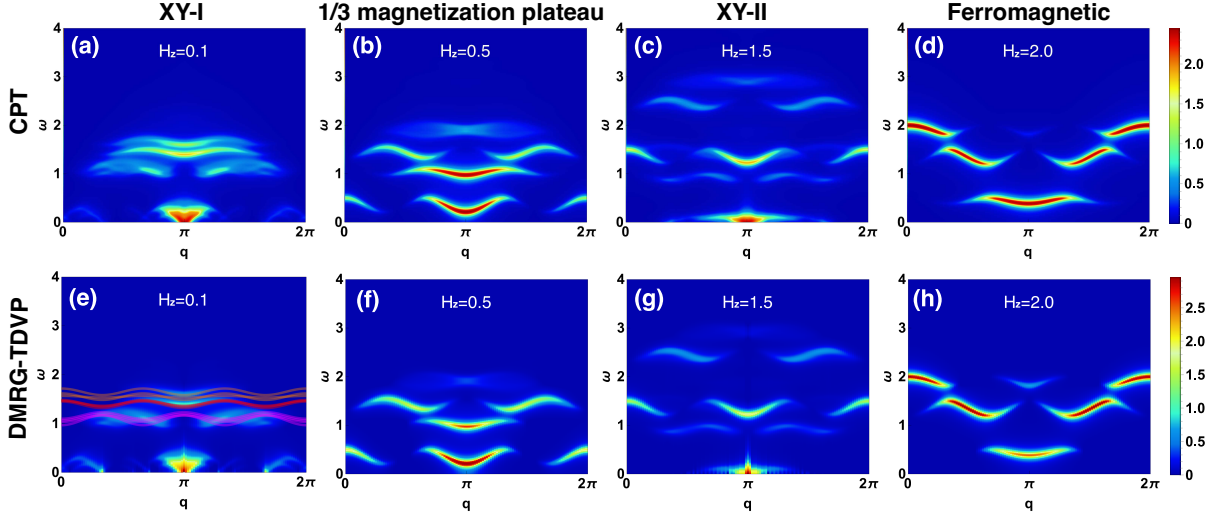


FIG. 3. $S^{xx}(q, \omega)$ obtained from CPT and DMRG-TDVP calculations for different phases with weak inter-trimer interaction. $S^{xx}(q, \omega)$ in (a)(e) XY-I phase, (b)(f) 1/3 magnetization plateau phase, (c)(g) XY-II phase, and (d)(h) Ferromagnetic phase. All results are from the case where $g = 0.3$, and the DMRG-TDVP calculations are from the length $L = 120$. The color coding of $S^{xx}(q, \omega)$ uses a piecewise function with the boundary value $U_0 = 2$.

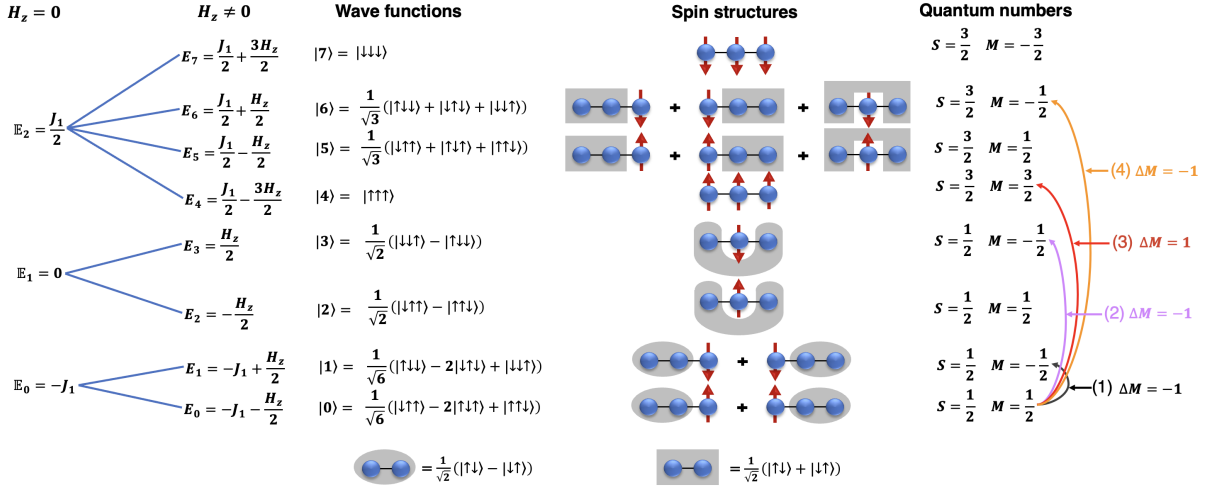


FIG. 4. The level spectrum, wave functions and quantum numbers of one isolated trimer under a longitudinal magnetic field. The second column lists the wave functions in the spin- z basis, while the third column presents the spin structures using a basis of singlets (gray ovals and rounded shapes), zero-magnetization triplets (gray square shapes), and unpaired spins (arrows). The last column lists the total spin quantum number S , magnetic quantum number M , and the internal trimer excitations with $\Delta M = \pm 1$.

instructive to analyze the complete level spectrum and corresponding eigenvectors of a single trimer. As depicted in Fig. 4, the application of a magnetic field results in the splitting of three energy levels into eight levels. Notably, the eigenvectors, spin quantum numbers and magnetic quantum numbers remain invariant. When $H_z \leq 1.5$, the ground state of one trimer is denoted as $|0\rangle$ with the energy $E_0 = -J_1 - H_z/2$. Considering the excitations with $|\Delta M| = 1$ from $|0\rangle$, only four cases satisfy this condition as indicated in the last column of Fig. 4. For small g , the coupling between trimers can be treated

as a perturbation of product state of isolated trimers, which has been confirmed in our previous study of trimer chain without the magnetic field [11]. Here, the perturbative analysis is still an effective tool to handle with the spin excitations of trimer chain under the magnetic field, particularly in the XY-I and 1/3 magnetization plateau phases. In the XY-I phase with small g , a weak magnetic field induces an incommensurate ground state with slight magnetization. By using the ground state $|0\rangle$ and first excited state $|1\rangle$ of single trimer, we can construct an approximate ground state with the antiferromagnetic

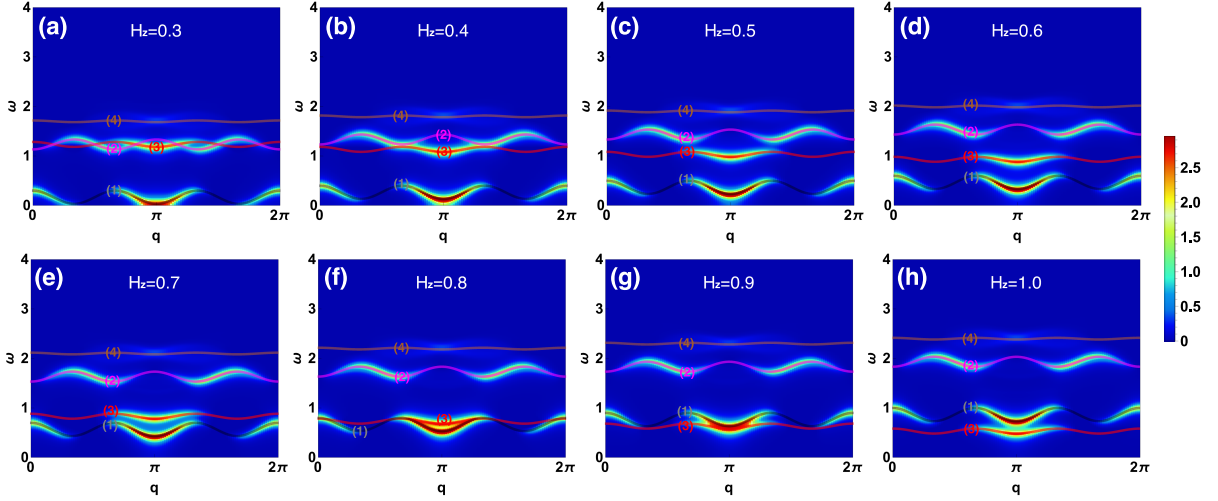


FIG. 5. $\mathcal{S}^{xx}(q, \omega)$ in $1/3$ magnetization plateau phase. All results are obtained by DMRG-TDVP calculations for $L = 120$, and the color coding of $\mathcal{S}^{xx}(q, \omega)$ uses a piecewise function with the boundary value $U_0 = 2$. The dispersion lines with colors and numbers are corresponding to the different localized excitations in a single trimer. (1)(2)(4) are the excitations from $|0\rangle \rightarrow |1\rangle$, $|0\rangle \rightarrow |3\rangle$ and $|0\rangle \rightarrow |6\rangle$ with $\Delta M = -1$, respectively. (3) is the excitations from $|0\rangle \rightarrow |4\rangle$ with $\Delta M = 1$.

order, such as $|\psi\rangle_g = |0101\dots 01\rangle$. Consequently, we are able to calculate the dispersion relations corresponding to the intermediate-energy and high-energy excitations with $|\Delta M| = 1$ by employing only $N = 4$ trimers, details can be found in the Supplementary note 6. Regarding the intermediate-energy excitations, four dispersion relations appear at $\omega \propto J_1$, as shown in Fig. 3(e), and describe the localized excitations from $|0\rangle$ to $|3\rangle$,

$$\epsilon_D(q) = \begin{cases} -\frac{1}{3}g \cos(3q) + E_1 - E_0 + H_z - \frac{1}{9}g, \\ -\frac{2}{9}g \cos(3q) + E_1 - E_0 + H_z, \\ -\frac{2}{9}g \cos(3q) + E_1 - E_0 + H_z + \frac{2}{9}g, \\ -\frac{2}{9}g \cos(3q) + E_1 - E_0 + H_z + \frac{2}{9}g. \end{cases} \quad (11)$$

It can be found that these dispersion relations depend on the gap $E_1 - E_0$ between the ground state and first excited state, and raise with the increase of magnetic field H_z . Comparing to the case $H_z = 0$ [11], only one branch of doublons is left under the effect of magnetic field, thus the intermediate-energy excitation corresponds to the generation of doublons. These dispersion lines are not well coincide with the spectrum due to the approximation of ground state. Additionally, we observe a continuum that may originate from the bound spinons. The central doublet dressed these spinons propagates through the system, resulting in various internal modes of these composite excitations, which in turn leads to a band of finite width in energy of these excitations, see the propagation of doublons in Supplementary note 2.

For the high-energy excitations, the magnetic field splits the spectrum into two branches as shown in Figs. 3(a)(e). Both branches arise from the high-energy

internal trimer excitations. We refer to the upper branch (excitation from $|0\rangle$ to $|6\rangle$) as the upper quarton, and the lower one (excitation from $|0\rangle$ to $|4\rangle$) as the lower quarton. The dispersion relations for the upper quarton are given by,

$$\epsilon_{\text{UQ}}(q) = \begin{cases} \frac{1}{18}g \cos(3q) + E_2 - E_0 + H_z - \frac{1}{6}g, \\ \frac{2}{9}g \cos(3q) + E_2 - E_0 + H_z - \frac{1}{6}g, \\ \frac{2}{9}g \cos(3q) + E_2 - E_0 + H_z + \frac{1}{6}g, \end{cases} \quad (12)$$

and the ones for lower quarton are given by,

$$\epsilon_{\text{LQ}}(q) = \begin{cases} \frac{1}{6}g \cos(3q) + E_2 - E_0 - H_z + \frac{1}{18}g, \\ \frac{2}{9}g \cos(3q) + E_2 - E_0 - H_z + \frac{1}{18}g, \\ \frac{2}{9}g \cos(3q) + E_2 - E_0 - H_z + \frac{1}{6}g. \end{cases} \quad (13)$$

These dispersion relations demonstrate a strong agreement with the DMRG-TDVP results regarding the location of these excitations and their band widths, which suggests that the picture of localized excitation is correct, although the calculation involves a very rough approximation of the ground state. Consequently, the high-energy quartons persist in this XY-I phase at small g .

In the $1/3$ magnetization plateau phase, each trimer possesses an effective magnetic quantum number $1/2$, resembling a polarized spin as a unit cell. We can construct the ground state of the $1/3$ magnetization plateau using the ground state of single trimer, $|\psi\rangle_g = |000\dots 00\rangle$, to study the spin dynamics. The low-energy spin wave arises from the flip of one spin in the ferromagnetic state,

which is well captured by the propagation of magnon. In this scenario, we flip an effective spin of one trimer, for example, replace one trimer from $|0\rangle$ to $|1\rangle$ in state $|\psi\rangle_g$, that results in the dispersion relation,

$$\epsilon^{(1)}(q) = \frac{4}{9}g \cos(3q) + H_z - \frac{4}{9}g, \quad (14)$$

which coincides well with the low-energy excitation spectrum no matter how large the magnetic field is, see Fig. 5. We refer to this excitation as the reduced spin wave in spite of the conventional magnon picture. Moving on to the intermediate-energy excitations, where one trimer is excited from $|0\rangle$ to $|3\rangle$ with $\Delta M = 1$, the corresponding dispersion relation is

$$\epsilon^{(2)}(q) = -\frac{1}{3}g \cos(3q) + E_1 - E_0 + H_z - \frac{2}{9}g. \quad (15)$$

Here, the intermediate-energy mode is termed as the doublon rather than the magnon since it originates from the localized trimer excitation and possesses a higher gap than the low-energy magnon. For the high-energy excitations, two branches of excitation spectra arise, corresponding to the excitation $|0\rangle \rightarrow |6\rangle$ with $\Delta M = -1$ and $|0\rangle \rightarrow |4\rangle$ with $\Delta M = 1$. The respective dispersion relations are given by,

$$\epsilon^{(3)}(q) = \frac{1}{6}g \cos(3q) + E_2 - E_0 - H_z + \frac{1}{9}g, \quad (16)$$

$$\epsilon^{(4)}(q) = \frac{1}{18}g \cos(3q) + E_2 - E_0 + H_z - \frac{1}{3}g, \quad (17)$$

which are referred as the high-energy quartons. Notably, it can be observed that the reduced spin wave ($|0\rangle \rightarrow |1\rangle$), doublon ($|0\rangle \rightarrow |3\rangle$) and upper quarton ($|0\rangle \rightarrow |6\rangle$) share the same magnetization quantum number $\Delta M = -1$, and raise together as the magnetic field grows. Conversely, the lower quarton descends independently due to its distinct magnetization quantum number $\Delta M = 1$, ultimately becoming the low-energy spectrum when $H_z \geq 0.9$. More interestingly, from Figs. 3(c)(g), we can observe that even in the XY-II phase, the excitations with $\Delta M = -1$ are still present in the high-energy regime.

III. QUANTUM MAGNETS

It has been discovered that $\text{Na}_2\text{Cu}_3\text{Ge}_4\text{O}_{12}$ serves as an excellent realization of the spin-1/2 Heisenberg antiferromagnetic trimer chain, where Cu_3O_8 constitutes the trimers formed by three edge-sharing CuO_4 square planes linearly. The magnetic Cu^{2+} ions within the CuO_4 square planes exhibit quantum spin-1/2 [12, 60]. Fig. 6(a) illustrates the simplified spin model, which includes an additional next-nearest neighbor intratrimer exchange coupling J_3 . The Hamiltonian for this system

is given by

$$\mathcal{H}' = \sum_{i=1}^N [J_1 (\mathbf{S}_{i,a} \cdot \mathbf{S}_{i,b} + \mathbf{S}_{i,b} \cdot \mathbf{S}_{i,c}) + J_2 \mathbf{S}_{i,c} \cdot \mathbf{S}_{i+1,a} + J_3 \mathbf{S}_{i,a} \cdot \mathbf{S}_{i,c}] - H_z \sum_{j=1}^{3N} S_j^z, \quad (18)$$

where the experimental measurements have determined the coupling strengths as $J_1 = 235\text{K}$ and $J_2 = J_3 = 0.18J_1$. In Fig. 6(b), the magnetic field splits the three energy levels of a single trimer into eight levels. When $H_z \leq 1.5$, the ground state is $|0\rangle$ with an energy of $E_0 = -0.955J_1 - H_z/2$. Although the antiferromagnetic interaction J_3 competes with the interaction J_1 and induces a frustration in the spin system, the frustrated trimer and isolated trimer share the same eigenfunctions and quantum numbers due to the small J_3 . Only the eigenenergies have little shifts, see Fig. 6(c). Therefore, the spin excitations are still described by the quasiparticles doublons and quartons. When $H_z = 0$, the eight energy levels (see Fig. 6(c)) only left three ones, $E'_0 = -0.955J_1$, $E'_1 = -0.135J_1$ and $E'_2 = 0.545J_1$. The doublon and quarton appear at $\omega \sim E'_1 - E'_0 = 0.82J_1$ and $\omega \sim E'_2 - E'_0 = 1.5J_1$, respectively, as shown in Fig. 6(e). In the inelastic neutron scattering measurements on $\text{Na}_2\text{Cu}_3\text{Ge}_4\text{O}_{12}$ [12], three excitation modes have been observed. The two-spinon modes are found below 5 meV, while, the doublon and quarton states appear at intermediate (17 – 22 meV) and high (32 – 37 meV) energy ranges, respectively, which are also revealed by the intermediate-energy (at $\omega \sim 0.82J_1$) and high-energy (at $\omega \sim 1.5J_1$) excitations in our numerical simulation. The trimer chain subject to J_3 interaction continues to exhibit the 1/3 magnetization plateau, as illustrated in Fig. 6(d). Experimental measurement has verified the existence of 1/3 magnetization plateau above 28 Tesla [12], which agrees with our DMRG calculation. Although the phase diagram and 1/3 magnetization plateau have been revealed [12], much less is known about the evolution of intermediate-energy and high-energy excitations under the magnetic field. In this subsection, we present the excitation spectrum of the model shown in Fig. 6(a), which is related to the material $\text{Na}_2\text{Cu}_3\text{Ge}_4\text{O}_{12}$. Due to the weak J_3 , the spin excitations in four phases displayed in Figs. 6(f)-(j) are also similar to those of trimer chain without J_3 , such as the separation of high-energy spectra, the gapless excitations in the XY-I and XY-II phases, the gap at the edges of Brillouin zones in the Ferromagnetic phase. Our theoretical results about the high-energy quasiparticles excitations under the magnetic field can be directly verified through the inelastic neutron scattering of the material $\text{Na}_2\text{Cu}_3\text{Ge}_4\text{O}_{12}$.

Moreover, BEC is a fascinating state of matter that has been observed in bosonic atoms and cold gases. Quasiparticles in the magnetic excitations with integer spin and Bose statistics, such as the magnon and triplon, also play a crucial role in investigating BEC [61–64]. Particu-

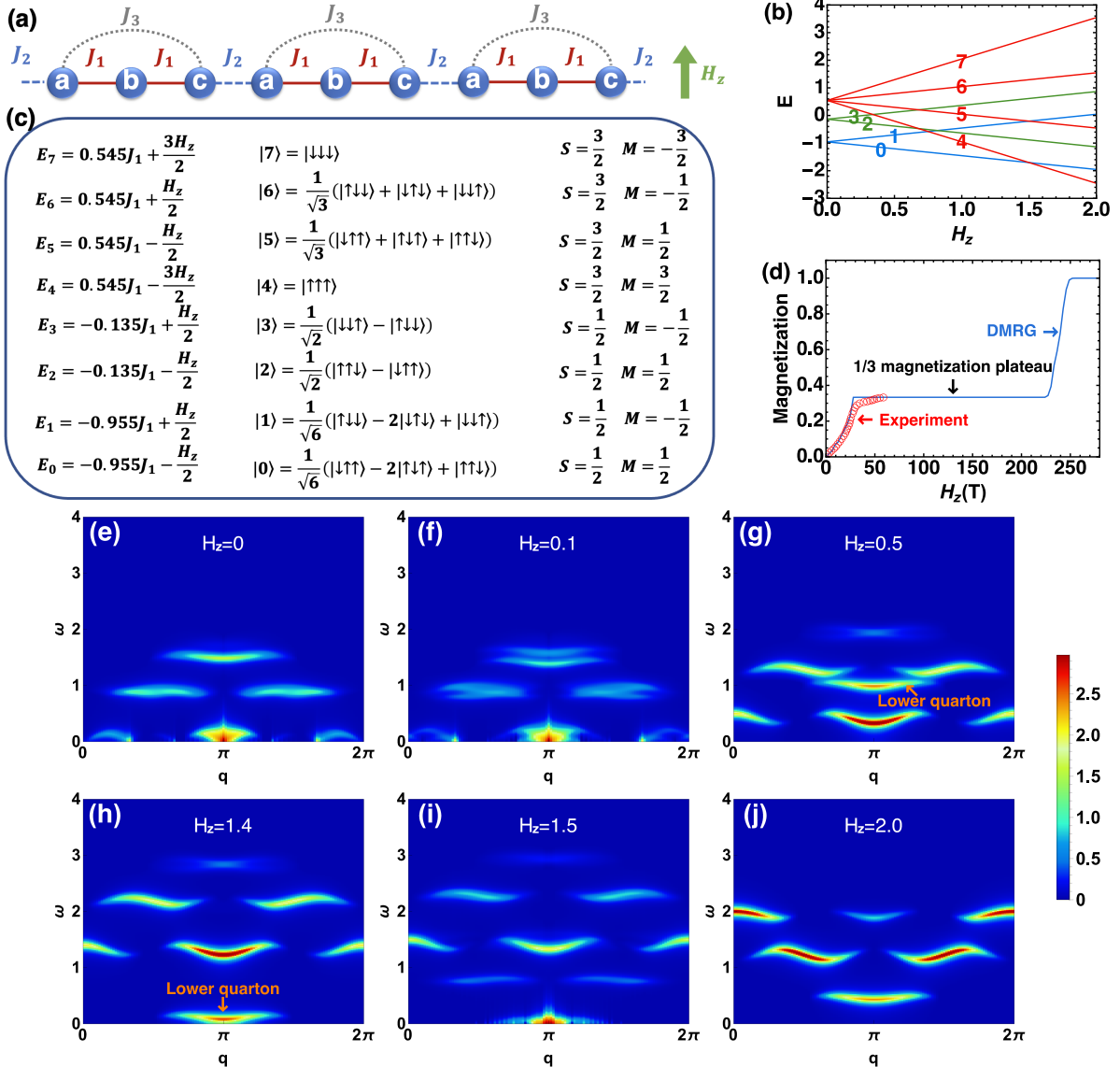


FIG. 6. **Trimer model related to the experimental material $\text{Na}_2\text{Cu}_3\text{Ge}_4\text{O}_{12}$.** (a) Schematic representation of trimer model with next-nearest neighbor intratrimer exchange couplings J_3 , and $J_2 = J_3 = 0.18J_1$. The spins a, b and c are the three Cu^{2+} spins within a trimer unit. (b) Energy levels as functions of magnetic field H_z . (c) Eigenenergies, wave functions, and quantum numbers of an isolated trimer unit in the material under the magnetic field H_z . (d) The magnetization curves obtained by experimental measurement and DMRG calculation, where the results have been normalized using the maximum of magnetization. The experimental data is extracted from Fig.1d in Ref.[12]. $S^{xx}(q, \omega)$ of spin model related to experimental materials $\text{Na}_2\text{Cu}_3\text{Ge}_4\text{O}_{12}$ in (e) the case without magnetic field, (f) XY-I phase, (g)(h) 1/3 magnetization plateau phase, (i) XY-II phase, and (j) Ferromagnetic phase obtained by DMRG-TDVP calculation for $L = 120$. The color coding of $S^{xx}(q, \omega)$ uses a piecewise function with the boundary value $U_0 = 2$.

larly in the dimerized antiferromagnets, such as TlCuCl_3 , the intradimer interaction is the stronger than the interdimer one, thereby an isolated dimer has a singlet ground state with total spin $S = 0$ and a triplet excited state with spin $S = 1$. Due to the weak interdimer interaction, the magnetic excitations are dominated by triplons. When a magnetic field is applied, the Zeeman term controls the density of triplons, causing the triplon with a magnetic quantum number $S^z = 1$ to decrease in

energy. At a critical magnetic field H_{C1} , the energy of the triplons reaches zero, and they gradually condense in the ground state until the another critical magnetic field H_{C2} is reached. Beyond H_{C2} , all spins become polarized.

Considering the characteristics of triplon BEC mentioned above, it is natural to ask that whether quorton BEC can be observed in trimerized systems. Here, we provide a simple analysis of the quorton BEC based on our results. Firstly, the high-energy quartons stem from

the internal trimer excitation, and possess an integer spin quantum number $S = 1$, satisfying the Bose statistics. Secondly, the magnetic field brings the lower branch of quartons closer to zero energy, as shown in Fig. 5 and Figs. 6(g)(h). At the critical point H_{C1} , which separates the $1/3$ magnetization plateau phase and XY-II phase, the lower quartons begin to condense and accumulate as the magnetic field increases in the XY-II phase. Furthermore, although the BEC has been observed in the real materials featuring the 3D spin systems, the 1D and 2D limits provide good starting points for understanding the field-induced quasiparticle BEC [63–66]. In the realm of 1D systems, it is well-established that BEC does not materialize due to the pronounced quantum fluctuations. Transitioning to 2D systems, the existence of a finite density of states at zero energy acts as a barrier to the formation of BEC. However, the critical exponents of the 1D or 2D quantum critical points can be observed over a quite large window of temperatures. In addition, the critical scaling exponent ν , governing the correlation length $\xi \sim |H - H_c|^{-\nu}$, remains constant at $1/2$ independent of spatial dimensionality [63]. In the study of 2D quantum dimer magnet, both critical fields, as well as critical temperatures of the BEC dome, can be accurately captured [66]. Therefore, the studies of 1D and 2D systems are valuable for the discovery of quasiparticle BEC. Our recent examination of spin dynamics in 2D trimer systems has unveiled the emergence of high-energy quartons [36]. These 2D trimer systems provide useful platforms to further study the quarton BEC. Moreover, a small but finite interlayer coupling in a quasi-2D magnet stabilizes marginal BEC [64]. The presence of quarton can be identified through inelastic neutron scattering experiments conducted on $\text{Na}_2\text{Cu}_3\text{Ge}_4\text{O}_{12}$, owing to the relatively weak interlayer coupling in comparison to the intratrimer interaction [12]. Consequently, there exists a significant possibility that field-induced quarton BEC will manifest in the quantum material $\text{Na}_2\text{Cu}_3\text{Ge}_4\text{O}_{12}$. Theoretically, it is interesting to search for more evidences of quarton BEC by exploring the (T, H_z) phase diagram and the power-law temperature dependence of thermodynamic properties for the 2D and 3D trimer systems in the future study.

IV. DISCUSSION

In summary, we have investigated the quantum phase transition and spin dynamics of the antiferromagnetic trimer chain in a longitudinal magnetic field by employing the ED, CPT and DMRG-TDVP methods. We have demonstrated that the interplay of magnetic field and interaction leads to the four distinct phases: XY-I, $1/3$ magnetization plateau, XY-II, and ferromagnetic phases. By mapping the entanglement entropy onto the parameter space (g, H_z) , we have obtained a detailed phase diagram, and confirmed that the critical phases XY-I and XY-II phases are both described by the conformal

field theory with the central charge $c \simeq 1$. The transitions between these phases are the second-order quantum phase transitions.

In the transverse and longitudinal excitations of trimer chain with magnetic field, we have identified that the incommensurate wave numbers of zero energy are dependent of the magnetization in the XY-I and XY-II phases. In addition, we have observed the presence of gapped excitations in both the $1/3$ magnetization plateau and ferromagnetic phases. Specifically, a continuum exists at the high-energy regime in the $1/3$ magnetization plateau phase. In the ferromagnetic phases, the excitation is still described by the spin waves, but magnons at the Brillouin zone edges exhibit two diverse energies for the same wave vector.

Furthermore, we have uncovered the intermediate-energy and high-energy excitations for small g , and have elucidated their excitation mechanisms in the XY-I and $1/3$ magnetization plateau phases by identifying their dispersion relations. In these phases, the intermediate-energy and high-energy modes correspond to the propagating internal trimer excitations known as doublons and quartons, respectively. Comparing to the trimer chain without magnetic field, the high-energy spectra split into two branches, corresponding to the upper quarton and lower quarton, respectively. As the magnetic field increases, the gap between these two branches widens, with the lower quarton becoming the low-energy spectrum.

Experimentally, there are already examples of coupled-trimer quantum magnets, such as $\text{A}_3\text{Cu}_3(\text{PO}_4)_4$ ($\text{A} = \text{Ca}, \text{Sr}, \text{Pb}$) [19–22] and $\text{Na}_2\text{Cu}_3\text{Ge}_4\text{O}_{12}$ [12]. Although the trimers in $\text{Pb}_3\text{Cu}_3(\text{PO}_4)_4$ do not exhibit a linear arrangement, two flat excitations at $\omega \sim 9\text{meV}$ and $\omega \sim 13.5\text{meV}$ have been observed in the inelastic neutron-scattering spectra measured at 8K [19]. These excitations are closely related to the intermediate-energy (at $\omega \sim J_1$) and high-energy (at $\omega \sim 1.5J_1$) excitations in the trimer chain without magnetic field [11]. Additionally, for the quantum magnet $\text{Na}_2\text{Cu}_3\text{Ge}_4\text{O}_{12}$, an additional next-neighbor interaction exists in the trimers, but its strength is weak, and the wave functions and quantum numbers of a single trimer remain invariant, thereby the doublons and quartons have been observed in the inelastic neutron-scattering experiments [12]. We have theoretically demonstrated that the doublons and quartons remain observable in the trimer chain under a magnetic field even when the interaction J_3 is introduced. These results can be directly examined in the inelastic neutron-scattering experiments measured on above quantum materials. Moreover, based on the results of the 1D trimer chain under a magnetic field, it is very likely that the quarton BEC may be identified in the experiments utilizing above materials. Our results will be valuable for interpreting inelastic neutron scattering and other experiments that probe the high-energy excitations beyond the spin waves and spinons, as well as for facilitating detailed investigations of coexisting exotic excitations.

V. METHODS

A. Matrix product states

DSF is an important physical quantity for studying the spin dynamics, which has been successfully facilitated by the DMRG along with the time evolution algorithms [38, 67–71]. In this article, we primarily employ the TDVP method to handle with the time evolution of many-body systems [40, 41]. Specifically, we perform the DMRG-TDVP calculations on a finite chain with open boundary condition to analyze the spectrum. We denote the ground state of trimer chain with magnetic field as $|\mathcal{G}\rangle$, then we can calculate the real time evolution of correlation function,

$$\langle \mathcal{G} | S_j^\alpha(t) S_0^\beta(0) | \mathcal{G} \rangle = e^{iE_0 t} \langle \mathcal{G} | S_j^\alpha e^{-i\mathcal{H}t} S_0^\beta | \mathcal{G} \rangle, \quad (19)$$

for various times t and distances j . E_0 represents the ground state energy, and we select the site in the middle of the chain as the site index 0. Firstly, we obtain the ground state $|\mathcal{G}\rangle$ in terms of a matrix product state (MPS) employing the DMRG method. Next, we apply the local perturbation \hat{S}_0^β in the middle of the spin chain to generate the initial state

$$|\phi\rangle = \hat{S}_0^\beta |\mathcal{G}\rangle \quad (20)$$

for real-time evolution. The real-time evolution state

$$|\phi(t)\rangle = e^{-i\mathcal{H}t} |\phi\rangle \quad (21)$$

is carried out using the single-site TDVP with a time step of $dt = 0.05J_1^{-1}$ and maximum time $t_{\max} = 200J_1^{-1}$. Finally, we perform a Fourier transformation to obtain $\mathcal{S}^{\alpha\beta}(q, \omega)$

$$\mathcal{S}^{\alpha\beta}(q, \omega) = \sum_j e^{-iqj} \left[\int_{-\infty}^{\infty} dt e^{i\omega t} \langle \hat{S}_j^\alpha(t) \hat{S}_0^\beta \rangle \right]. \quad (22)$$

Technically, in order to remove the constraint imposed by the finite-time limit on the resolution of the spectral functions in frequency space, we incorporate a Gaussian windowing function $\exp[-4(t/t_{\max})^2]$ in the reconstruction of the DSF [38]. During the DMRG calculation, we have set $\varepsilon_{\text{SVD}} = 10^{-11}$ and kept a maximum of 6000 states. The time evolution is performed on a chain with open boundary condition and $N = 120$ spins, which is sufficiently large to avoid finite-size effects, and the maximum bond dimension is set to 2000. All MPS simulations are carried out using the ITensor library [72].

B. Cluster perturbation theory

Cluster perturbation theory (CPT) is a theoretical framework used to study the electronic and magnetic properties of strongly correlated electrons [42–45], especially for calculating the single-particle spectral functions

of Hubbard-type fermionic models and the dynamical spin structure factors of Heisenberg models. The basic idea behind CPT is to divide a large system into smaller clusters, calculate the properties of these clusters exactly, and then use the mean-field and perturbation theory to infer the properties of the entire system. Here, we employ ED as a solver to calculate the dynamical spin structure factor within the cluster. Following Ref. 45, we give a brief overview of the steps involved in cluster perturbation theory for spin models.

Firstly, we transform the spin model into a hard-core boson model using the following mapping,

$$S_i^+ = b_i^\dagger, S_i^- = b_i, S_i^z = b_i^\dagger b_i - 1/2, \quad (23)$$

Then the Hamiltonian can be rewritten as,

$$\begin{aligned} \mathcal{H} = & \sum_{i=1}^N \left(\frac{J_1}{2} b_{i,a}^\dagger b_{i,b} + \frac{J_1}{2} b_{i,b}^\dagger b_{i,c} + \frac{J_2}{2} b_{i,c}^\dagger b_{i+1,a} + H.c. \right) \\ & + \sum_{i=1}^N [J_1 n_{i,a} n_{i,b} + J_1 n_{i,b} n_{i,c} + J_2 n_{i,c} n_{i+1,a}] \\ & - \left(H_z + \frac{J_1 + J_2}{2} \right) \sum_{i=1, i \in a/c}^N n_i \\ & - (H_z + J_1) \sum_{i=1, i \in b}^N n_i + \mathcal{H}_{\text{const.}}, \end{aligned} \quad (24)$$

where the b_i^\dagger , b_i and $n_i = b_i^\dagger b_i$ are the bosonic operators with hard-core constraint $n_i = 0$ or 1.

Secondly, we split the system into clusters. In our calculations, the cluster size is chosen to be $N = 8$, $L = 24$ which is large enough to get the accurate results. For the interaction bonds connecting nearby clusters. We use self-consistent mean-field treatment to decouple the interactions between clusters,

$$J_2 n_{1,c} n_{N,a} \approx J_2 (\langle n_{1,a} \rangle n_{N,c} + \langle n_{N,c} \rangle n_{1,a}). \quad (25)$$

Thirdly, we employ exact diagonalization to self-consistently obtain the mean-field potentials of two end sites, $\langle n_{1,c} \rangle$ and $\langle n_{N,c} \rangle$. And after the convergence, we run a ED simulation to obtain the real-frequency single-particle Green function matrix $\mathbf{G}_{ij}^C(\omega)$ using Lanczos iteration method, where C denotes the Green function matrix of cluster.

Fourthly, the original lattice Green function matrix can be obtained from the cluster Green function matrix by neglecting the nonlocal self-energy between clusters.

$$\mathbf{G}^{L,-1}(\tilde{q}, \omega) = \mathbf{G}^{C,-1}(\omega) - V(\tilde{q}). \quad (26)$$

where L denotes the Green function matrix of original lattice, $\tilde{\mathbf{q}}$ is the wave vector in the Brillouin zone of supercell form by the cluster.

Fifthly, we do the reperiodization of Green function matrix to restore the translational invariance.

$$G_{\text{CPT}}(q, \omega) = \frac{1}{N_s} \sum_{ij} e^{-i\mathbf{q}(\mathbf{r}_i - \mathbf{r}_j)} G_{ij}^L(\omega). \quad (27)$$

Then the transverse dynamical spin structure factor can be obtained via

$$S^{+-}(q, \omega) = -\frac{1}{\pi} \text{Im} G_{\text{CPT}}(q, \omega). \quad (28)$$

The cluster perturbation theory for spin models has been successfully applied to investigate the $J_1 - J_2$ and $J_1 - J_3$ models on 2D square lattice [45, 73], the $J_1 - J_2$ model on honeycomb lattice [74], as well as 2D trimer models [36]. This method proves effective in characterizing the continua in quantum spin liquid phases, as well as the magnon and triplon excitations in conventional Néel and valence bond solid phases. This method is exact in two limiting cases. One is the interactions between clusters tend towards zero or are extremely weak; Another is the cluster size approaches infinity or is very large. In the case of our trimer chain model, when $g = J_2/J_1$ is small, accurate results can be obtained even with very small clusters, such as $N = 2, 4$. The choice of a cluster size of $N = 8$ in our study ensures accuracy in both small and large g regimes. This cluster size proves sufficiently large to guarantee precision across a wide range of parameter values.

ACKNOWLEDGMENTS

We like to thank Zijian Xiong for fruitful discussions. This project is supported by the National Key R&D Program of China, Grants No. 2022YFA1402802, No. 2018YFA0306001, NSFC-92165204, NSFC-11974432, and Shenzhen Institute for Quantum Science and Engineering (Grant No. SIQSE202102). J.Q.C. is supported by the National Natural Science Foundation of China through Grants No. 12047562. H.Q.W.

is supported by the National Natural Science Foundation of China through Grants No. 11804401, No. 11832019 and the Guangzhou Basic and Applied Basic Research Foundation (202201011569). J.Q.C. also acknowledges the financial support from the Special Project in Key Areas for Universities in Guangdong Province (No. 2023ZDZX3054) and the Dongguan Key Laboratory of Artificial Intelligence Design for Advanced Materials (DKL-AIDAM).

VI. AUTHOR CONTRIBUTIONS

D.X.Y., H.Q.W., and J.Q.C. conceived and designed the project. J.Q.C., H.Q.W. and Z.Y.N. performed the numerical simulations. J.Q.C., H.Q.W., Z.Y.N., and D.X.Y. provided the explanation of the numerical results. All authors contributed to the discussion of the results and wrote the paper.

VII. DATA AVAILABILITY

The data that support the findings of this study are available from the corresponding authors upon reasonable request.

VIII. CODE AVAILABILITY

The code used for the analysis is available from the authors upon reasonable request.

IX. COMPETING INTERESTS

The authors declare no competing interests.

-
- [1] Mikeska, H.-J. & Kolezhuk, A. K. *One-dimensional magnetism*, 1–83 (Springer Berlin Heidelberg, Berlin, Heidelberg, 2004).
- [2] Karbach, M., Müller, G., Bougourzi, A. H., Fledderjohann, A. & Mütter, K.-H. Two-spinon dynamic structure factor of the one-dimensional $S = 1/2$ Heisenberg antiferromagnet. *Phys. Rev. B* **55**, 12510–12517 (1997).
- [3] Tennant, D. A., Perring, T. G., Cowley, R. A. & Nagler, S. E. Unbound spinons in the $S = 1/2$ antiferromagnetic chain KCuF_3 . *Phys. Rev. Lett* **70**, 4003 (1993).
- [4] Lake, B. *et al.* Multispinon continua at zero and finite temperature in a near-ideal Heisenberg chain. *Phys. Rev. Lett.* **111**, 137205 (2013).
- [5] Enderle, M. *et al.* Two-spinon and four-spinon continuum in a frustrated ferromagnetic spin-1/2 chain. *Phys. Rev. Lett.* **104**, 237207 (2010).
- [6] Klauser, A., Mossel, J., Caux, J.-S. & van den Brink, J. Spin-exchange dynamical structure factor of the $S = 1/2$ Heisenberg chain. *Phys. Rev. Lett.* **106**, 157205 (2011).
- [7] Schlappa, J. *et al.* Probing multi-spinon excitations outside of the two-spinon continuum in the antiferromagnetic spin chain cuprate Sr_2CuO_3 . *Nat. Commun.* **9**, 5394 (2018).
- [8] Kohno, M. Dynamically dominant excitations of string solutions in the spin-1/2 antiferromagnetic Heisenberg chain in a magnetic field. *Phys. Rev. Lett.* **102**, 037203 (2009).
- [9] Wang, Z. *et al.* Experimental observation of Bethe strings. *Nature* **554**, 219–223 (2018).
- [10] Wang, Z. *et al.* Quantum critical dynamics of a Heisenberg-Ising chain in a longitudinal field: Many-body strings versus fractional excitations. *Phys. Rev. Lett.* **123**, 067202 (2019).
- [11] Cheng, J.-Q. *et al.* Fractional and composite excitations of antiferromagnetic quantum spin trimer chains. *npj Quantum Mater.* **7**, 1–11 (2022).
- [12] Bera, A. K. *et al.* Emergent many-body composite excitations of interacting spin-1/2 trimers. *Nat. Commun.* **13**, 6888 (2022).
- [13] Do, S.-H. *et al.* Understanding temperature-dependent $S(3)$ spin dynamics in the $S = 1$ antiferromagnet $\text{Ba}_2\text{FeSi}_2\text{O}_7$. *npj Quantum Mater.* **8**, 5 (2023).

- [14] Han, J.-H. *et al.* Weak-coupling to strong-coupling quantum criticality crossover in a kitaev quantum spin liquid α -RuCl₃. *npj Quantum Mater.* **8**, 33 (2023).
- [15] Dagotto, E. & Rice, T. M. Surprises on the way from one- to two-dimensional quantum magnets: The ladder materials. *Science* **271**, 618 (1996).
- [16] Haldane, F. D. M. Continuum dynamics of the 1-D Heisenberg antiferromagnet: Identification with the $\phi(3)$ nonlinear sigma model. *Phys. Lett. A* **93**, 464–468 (1983).
- [17] Schmidiger, D. *et al.* Symmetric and asymmetric excitations of a strong-leg quantum spin ladder. *Phys. Rev. B* **88**, 094411 (2013).
- [18] Doretto, R. L. & Vojta, M. Quantum magnets with weakly confined spinons: Multiple length scales and quantum impurities. *Phys. Rev. B* **80**, 024411 (2009).
- [19] Matsuda, M. *et al.* Magnetic excitations from the linear Heisenberg antiferromagnetic spin trimer system $A_3Cu_3(PO_4)_4$ ($A = Ca, Sr$, and Pb). *Phys. Rev. B* **71**, 144411 (2005).
- [20] Drillon, M. *et al.* 1D ferrimagnetism in copper (ii) trimetric chains: specific heat and magnetic behavior of $A_3Cu_3(PO_4)_4$ with $A = Ca, Sr$. *J. Magn. Magn. Mater.* **128**, 83–92 (1993).
- [21] Belik, A. A., Matsuo, A., Azuma, M., Kindo, K. & Takano, M. Long-range magnetic ordering of $s = 1/2$ linear trimers in $A_3Cu_3(PO_4)_4$ ($A = Ca, Sr, Pb$). *J. Solid State Chem.* **178**, 709–714 (2005).
- [22] Yamamoto, S. & Ohara, J. Low-energy structure of the homometallic intertwining double-chain ferrimagnets $A_3Cu_3(PO_4)_4$ ($A = Ca, Sr, Pb$). *Phys. Rev. B* **76**, 014409 (2007).
- [23] Montenegro-Filho, R. R., Matias, F. S. & Coutinho-Filho, M. D. Topology of many-body edge and extended quantum states in an open spin chain: $1/3$ plateau, Kosterlitz-Thouless transition, and Luttinger liquid. *Phys. Rev. B* **102**, 035137 (2020).
- [24] Montenegro-Filho, R. R., Silva-Júnior, E. J. P. & Coutinho-Filho, M. D. Ground-state phase diagram and thermodynamics of coupled trimer chains. *Phys. Rev. B* **105**, 134423 (2022).
- [25] Hasegawa, Y. & Matsumoto, M. Magnetic excitation in interacting spin trimer systems investigated by extended spin-wave theory. *J. Phys. Soc. Jpn.* **81**, 094712 (2012).
- [26] Cao, G. *et al.* Quantum liquid from strange frustration in the trimer magnet $Ba_4Ir_3O_{10}$. *npj Quantum Mater.* **5**, 26 (2020).
- [27] Shen, Y. *et al.* Emergence of spinons in layered trimer Iridate $Ba_4Ir_3O_{10}$. *Phys. Rev. Lett.* **129**, 207201 (2022).
- [28] Headings, N. S., Hayden, S. M., Coldea, R. & Perring, T. G. Anomalous high-energy spin excitations in the High- T_c superconductor-parent antiferromagnet La_2CuO_4 . *Phys. Rev. Lett.* **105**, 247001 (2010).
- [29] Zhou, K.-J. *et al.* Persistent high-energy spin excitations in iron-pnictide superconductors. *Nat. Commun.* **4**, 1470 (2013).
- [30] Ishii, K. *et al.* High-energy spin and charge excitations in electron-doped copper oxide superconductors. *Nat. Commun.* **5**, 3714 (2014).
- [31] Wakimoto, S. *et al.* High-energy magnetic excitations in overdoped $La_{2-x}Sr_xCuO_4$ studied by neutron and resonant inelastic X-ray scattering. *Phys. Rev. B* **91**, 184513 (2015).
- [32] Song, Y. *et al.* High-energy magnetic excitations from heavy quasiparticles in $CeCu_2Si_2$. *npj Quantum Mater.* **6**, 60 (2021).
- [33] Shao, H. *et al.* Nearly deconfined spinon excitations in the square-lattice spin-1/2 Heisenberg antiferromagnet. *Phys. Rev. X* **7**, 041072 (2017).
- [34] Dalla Piazza, B. *et al.* Fractional excitations in the square-lattice quantum antiferromagnet. *Nat. Phys.* **11**, 62–68 (2015).
- [35] Gu, C., Gu, Z.-L., Yu, S.-L. & Li, J.-X. Spectral evolution of the $s = \frac{1}{2}$ antiferromagnetic Heisenberg model: From one to two dimensions. *Phys. Rev. B* **108**, 224418 (2023).
- [36] Chang, Y.-Y., Cheng, J.-Q., Shao, H., Yao, D.-X. & Wu, H.-Q. Magnon, doublon and quarton excitations in 2D trimerized Heisenberg models. *arXiv* **2401.00376** (2023).
- [37] White, S. R. Density matrix formulation for quantum renormalization groups. *Phys. Rev. Lett.* **69**, 2863–2866 (1992).
- [38] White, S. R. & Feiguin, A. E. Real-time evolution using the density matrix renormalization group. *Phys. Rev. Lett.* **93**, 076401 (2004).
- [39] Schollwöck, U. The density-matrix renormalization group in the age of matrix product states. *Ann. Phys.* **326**, 96 – 192 (2011).
- [40] Haegeman, J. *et al.* Time-dependent variational principle for quantum lattices. *Phys. Rev. Lett.* **107**, 070601 (2011).
- [41] Haegeman, J., Lubich, C., Oseledets, I., Vandereycken, B. & Verstraete, F. Unifying time evolution and optimization with matrix product states. *Phys. Rev. B* **94**, 165116 (2016).
- [42] Gros, C. & Valentí, R. Cluster expansion for the self-energy: A simple many-body method for interpreting the photoemission spectra of correlated fermi systems. *Phys. Rev. B* **48**, 418–425 (1993).
- [43] Sénéchal, D., Perez, D. & Pioro-Ladrière, M. Spectral weight of the hubbard model through cluster perturbation theory. *Phys. Rev. Lett.* **84**, 522–525 (2000).
- [44] Maier, T., Jarrell, M., Pruschke, T. & Hettler, M. H. Quantum cluster theories. *Rev. Mod. Phys.* **77**, 1027–1080 (2005).
- [45] Yu, S.-L., Wang, W., Dong, Z.-Y., Yao, Z.-J. & Li, J.-X. Deconfinement of spinons in frustrated spin systems: Spectral perspective. *Phys. Rev. B* **98**, 134410 (2018).
- [46] Amico, L., Fazio, R., Osterloh, A. & Vedral, V. Entanglement in many-body systems. *Rev. Mod. Phys.* **80**, 517–576 (2008).
- [47] Laflorencie, N. Quantum entanglement in condensed matter systems. *Phys. Rep.* **646**, 1–59 (2016). Quantum entanglement in condensed matter systems.
- [48] Cheng, J.-Q., Wu, W. & Xu, J.-B. Multipartite entanglement in an XXZ spin chain with Dzyaloshinskii–Moriya interaction and quantum phase transition. *Quantum Inf. Process.* **16**, 1–20 (2017).
- [49] Goldstein, M. & Sela, E. Symmetry-resolved entanglement in many-body systems. *Phys. Rev. Lett.* **120**, 200602 (2018).
- [50] Cheng, J.-Q. & Xu, J.-B. Multipartite entanglement, quantum coherence, and quantum criticality in triangular and Sierpiński fractal lattices. *Phys. Rev. E* **97**, 062134 (2018).
- [51] Kunkel, P. *et al.* Detecting entanglement structure in continuous many-body quantum systems. *Phys. Rev. Lett.* **128**, 020402 (2022).

- [52] Oshikawa, M., Yamanaka, M. & Affleck, I. Magnetization plateaus in spin chains: “Haldane gap” for half-integer spins. *Phys. Rev. Lett.* **78**, 1984–1987 (1997).
- [53] Sakai, T. & Okamoto, K. Quantum magnetization plateaus of an anisotropic ferrimagnetic spin chain. *Phys. Rev. B* **65**, 214403 (2002).
- [54] Calabrese, P., Campostrini, M., Essler, F. & Nienhuis, B. Parity effects in the scaling of block entanglement in gapless spin chains. *Phys. Rev. Lett.* **104**, 095701 (2010).
- [55] D’Emidio, J., Block, M. S. & Kaul, R. K. Rényi entanglement entropy of critical $SU(N)$ spin chains. *Phys. Rev. B* **92**, 054411 (2015).
- [56] Feng, S., Alvarez, G. & Trivedi, N. Gapless to gapless phase transitions in quantum spin chains. *Phys. Rev. B* **105**, 014435 (2022).
- [57] Hallberg, K., Wang, X. Q. G., Horsch, P. & Moreo, A. Critical behavior of the $S = 3/2$ antiferromagnetic heisenberg chain. *Phys. Rev. Lett.* **76**, 4955–4958 (1996).
- [58] Takayoshi, S. *et al.* Phase transitions and spin dynamics of the quasi-one dimensional ising-like antiferromagnet $BaCo_2V_2O_8$ in a longitudinal magnetic field. *Phys. Rev. Res.* **5**, 023205 (2023).
- [59] Wang, Z. *et al.* From confined spinons to emergent fermions: Observation of elementary magnetic excitations in a transverse-field ising chain. *Phys. Rev. B* **94**, 125130 (2016).
- [60] Yasui, Y., Kawamura, Y., Kobayashi, Y. & Sato, M. Magnetic and dielectric properties of one-dimensional array of $S = 1/2$ linear trimer system $Na_2Cu_3Ge_4O_{12}$. *J. Appl. Phys.* **115**, 17E125 (2014).
- [61] Rüegg, C. *et al.* Bose–Einstein condensation of the triplet states in the magnetic insulator $TiCuCl_3$. *Nature* **423**, 62–65 (2003).
- [62] Giamarchi, T., Rüegg, C. & Tchernyshyov, O. Bose–Einstein condensation in magnetic insulators. *Nat. Phys.* **4**, 198–204 (2008).
- [63] Zapf, V., Jaime, M. & Batista, C. Bose–Einstein condensation in quantum magnets. *Rev. Mod. Phys.* **86**, 563 (2014).
- [64] Matsumoto, Y. *et al.* A quantum critical bose gas of magnons in the quasi-two-dimensional antiferromagnet $YbCl_3$ under magnetic fields. *Nat. Phys.* 1–8 (2024).
- [65] Volkov, P. A., Gazit, S. & Pixley, J. H. Magnon Bose–Einstein condensation and superconductivity in a frustrated kondo lattice. *Proc. Nat. Acad. Sci.* **117**, 20462–20467 (2020).
- [66] Feng, C., Stoudenmire, E. M. & Wietek, A. Bose–Einstein condensation in honeycomb dimer magnets and $Yb_2Si_2O_7$. *Phys. Rev. B* **107**, 205150 (2023).
- [67] Barthel, T., Schollwöck, U. & White, S. R. Spectral functions in one-dimensional quantum systems at finite temperature using the density matrix renormalization group. *Phys. Rev. B* **79**, 245101 (2009).
- [68] Bruognolo, B., Weichselbaum, A., von Delft, J. & Garst, M. Dynamic structure factor of the spin- $\frac{1}{2}$ XXZ chain in a transverse field. *Phys. Rev. B* **94**, 085136 (2016).
- [69] Paeckel, S. *et al.* Time-evolution methods for matrix-product states. *Ann. Phys.* **411**, 167998 (2019).
- [70] Keselman, A., Balents, L. & Starykh, O. A. Dynamical signatures of quasiparticle interactions in quantum spin chains. *Phys. Rev. Lett.* **125**, 187201 (2020).
- [71] Drescher, M., Vanderstraeten, L., Moessner, R. & Pollmann, F. Dynamical signatures of symmetry-broken and liquid phases in an $s = \frac{1}{2}$ Heisenberg antiferromagnet on the triangular lattice. *Phys. Rev. B* **108**, L220401 (2023).
- [72] Fishman, M., White, S. R. & Stoudenmire, E. M. The ITensor Software Library for Tensor Network Calculations. *SciPost Phys. Codebases* 4 (2022).
- [73] Wu, M., Gong, S.-S., Yao, D.-X. & Wu, H.-Q. Phase diagram and magnetic excitations of $J_1 - J_3$ Heisenberg model on the square lattice. *Phys. Rev. B* **106**, 125129 (2022).
- [74] Gu, C., Yu, S.-L. & Li, J.-X. Spin dynamics and continuum spectra of the honeycomb $J_1 - J_2$ antiferromagnetic Heisenberg model. *Phys. Rev. B* **105**, 174403 (2022).

Supplementary Note 1: Spin-spin correlation function of ground state

In main text, we have provided the magnetization curves, entanglement entropy, and central charge as evidences supporting the existence of four distinct phases: XY-I, 1/3 magnetization plateau, XY-II, and ferromagnetic phases. Here, to characterize these phases, we utilize the spin-spin correlation function of the ground state denoted as $\langle S_0^x S_j^x \rangle$, as illustrated in the Supplementary Fig. 7. In the XY-I and XY-II phases, magnetic ordering is absent in the ground state, and the spin correlation functions decay according to the power laws $\langle S_0^x S_j^x \rangle \sim j^{-\eta}$ with $\eta_1 \simeq 0.995$ and $\eta_2 \simeq 0.937$. These two critical exponents both approach to 1, which are similar to the $S = 1/2$ isotropic Heisenberg chain [57]. In the 1/3 magnetization plateau phase, $\langle S_0^x S_j^x \rangle$ quickly decays to zero as a function of the distance, while in the ferromagnetic phase, $\langle S_0^x S_j^x \rangle$ are zero for all distances. Therefore, the spin-spin correlation function $\langle S_0^x S_j^x \rangle$ serves as a valuable tool for distinguishing between the magnetically ordered phases and critical phases within this trimer spin chain subject to a magnetic field.

Supplementary Note 2: Spin dynamics without the magnetic field

In our previous investigation [11], we have explored the spin dynamics of trimer chain without magnetic field by using the quantum Monte Carlo with subsequent numerical analytic continuation (QMC-SAC). We have showed that small intertrimer interaction gives rise to distinct types of collective excitations associated with the internal trimer excitations. Particularly in the intermediate-energy and high-energy regimes, the presence of doublons and quartons have been unveiled through the QMC-SAC calculation and theoretical analysis. These findings have been verified from the inelastic neutron scattering measurements on $\text{Na}_2\text{Cu}_3\text{Ge}_4\text{O}_{12}$ [12], where the trimer chain subject to the next-nearest neighbor intratrimer exchange couplings J_3 , as depicted in Fig.6(a) of main text. The J_3 interaction induces the frustration in each trimer, potentially leading to a negative sign problem in the QMC-SAC calculation. Therefore, we mainly employ the density matrix renormalization group and time-dependent variational principle (DMRG-TDVP) to investigate the spin dynamics of trimer systems under a magnetic field. Supplementary Fig. 8 presents the results of spin dynamics $\mathcal{S}(q, \omega) = 3\mathcal{S}^{xx}(q, \omega)$ for $g = 0.1$ obtained through the QMC-SAC, DMRG-TDVP and CPT calculations, where the trimer chain without magnetic field preserving the $\text{SU}(2)$ symmetry has been considered. All three methods successfully reveal the low-energy continuum, intermediate-energy and high-energy excitations, corresponding to the spinon, doublon and quarton, respectively. Only have little differences on some details of the spectra. For example, the QMC-SAC calculation effectively characterized the spinon continuum with high resolution in the low-energy regime. In contrast,

the DMRG-TDVP and CPT calculations distinctly separated the doublons and quartons in the intermediate-energy and high-energy regimes. These methods offer reliable results for exploring the spin dynamics of trimer chain.

In order to further understanding the propagation of doublons and quartons, we provide a physical elucidation in Supplementary Fig. 9. Let us first consider the doublon excitation, as depicted in Supplementary Fig. 9(a), one trimer is excited to its second-excited doublet with a flipped effective spin, including an excitation characterized by $|\Delta M| = 1$ and the formation of two domain walls. These mobile domain walls, termed spinons, though not entirely free, remain tethered to the persistent central doublet. Consequently, the central doublet propagates through the system dressed by spinons, giving rise to numerous internal modes within these composite excitations, thereby engendering a band of finite width. Next, we turn to the quarton, which offers several possibilities for creating the excitation with $|\Delta M| = 1$ according to the trimer excitations. For simplicity, we consider two cases based on the $S^z = 3/2$ states to introduce the propagation of quartons with and without domain walls. In Supplementary Fig. 9(b), an effective spin $S^z = -1/2$ is replaced by the $S^z = 3/2$ state, then an excitation $|\Delta M| = 2$ is generated. To achieve the excitation $|\Delta M| = 1$, we have to flip one of neighbor $S^z = 1/2$ spins down, which creates a domain wall. On the other side of the excited trimer, a domain wall may also propagate outward. Thus, the central excited state propagates throughout the system enveloped by two domain walls. In Supplementary Fig. 9(c), the replacement of an effective spin $S^z = 1/2$ with the $S^z = 3/2$ state leads to the presence of two domain walls, but disappear during the propagation of central excited state. Then a quarton propagates without domain walls. If we restore spin-rotation symmetry and exploring alternative scenarios, quartons emergence through analogous mechanisms. For further insights into the dynamics of doublons and quartons, we refer the interested reader to the Ref. [11].

Supplementary Note 3: Longitudinal excitation spectrum

Let us consider the longitudinal excitation spectrum $\mathcal{S}^{zz}(q, \omega)$ at $g = 0.8$ for XY-I phase, 1/3 magnetic plateau phase and XY-II phase. As shown in Supplementary Fig. 10, the excitations are gapless in two XY phases and gapped in the 1/3 magnetic plateau phase. For the ferromagnetic phase, all spins are polarized in the z direction, the longitudinal excitation spectrum in this phase is absent. In the XY-I and XY-II phases, the intraband zero-energy excitations correspond to the longitudinal fluctuations in terms of spinless fermion language [58]. The incommensurability appearing in the spin dynamics can be observed from the splitting of the bands. In the XY-I phase, see Supplementary Fig. 10(a), the longitudinal excitations conserve the total number of particles without

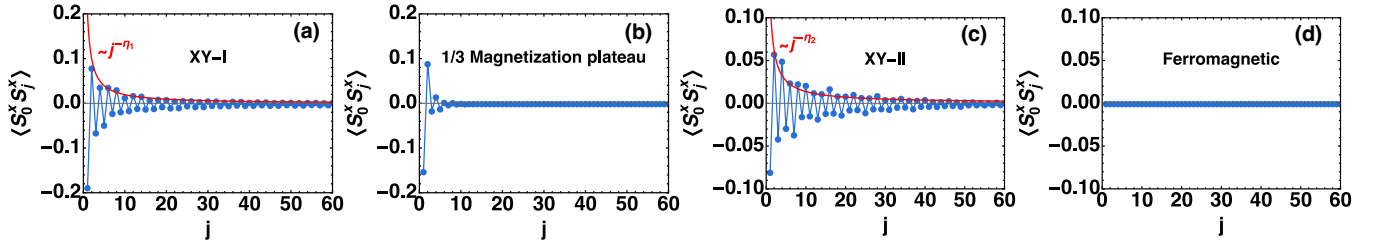


FIG. 7. Spin-spin correlation function of ground state $\langle S_0^x S_j^x \rangle$ obtained from DMRG calculations. $\langle S_0^x S_j^x \rangle$ as functions of distances between spins for (a) XY-I phase ($H_z = 0.2$), (b) 1/3 magnetization plateau phase ($H_z = 1.0$), (c) XY-II phase ($H_z = 1.5$), and (d) Ferromagnetic phase ($H_z = 2.0$). The red lines are the fits of correlation functions, $\langle S_0^x S_j^x \rangle \sim j^{-\eta}$, which indicates the correlation functions decay according to power laws with the critical exponents (a) $\eta_1 \simeq 0.995$ and (c) $\eta_2 \simeq 0.937$. All results are from the case where $g = 0.5$ and $L = 180$.

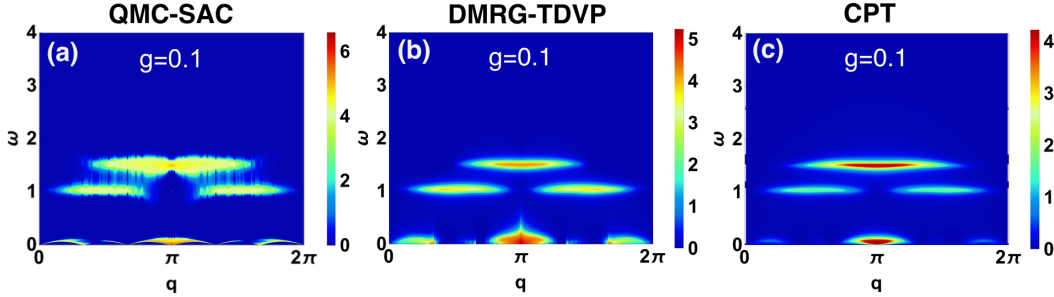


FIG. 8. Dynamic spin structure factor $\mathcal{S}(q, \omega)$ obtained from (a) QMC-SAC, (b) DMRG-TDVP and (c) CPT calculations for the trimer chain without magnetic field. The QMC-SAC data is sourced from our previous study [11]. The color coding of $\mathcal{S}(q, \omega)$ uses a piecewise function with the boundary value $U_0 = 4$. Below the boundary, the low-intensity portion is characterized by a linear mapping of the spectral function to the color bar, while above the boundary a logarithmic scale is used, $U = U_0 + \log_{10}[\mathcal{S}(q, \omega)] - \log_{10}(U_0)$.

changing the magnetization of ground state, which indicates that the incommensurate fluctuations reaching zero energy at $q = (1 \pm m_z)\pi$, where $m_z = 0.1111$ is the magnetization normalized by its saturation value. In the XY-II phase, see Supplementary Fig. 10(c), the incommensurate fluctuations reach the zero energy at $q = (1 \pm m_z)\pi$ where $m_z = 0.5697$.

Supplementary Note 4: Effects of intertrimer interaction on the spin dynamics

In the main text, we have discussed the effects of a magnetic field on the spin dynamics by considering a fixed value of g , how the spectra evolve for varying g will provide another insight to understand the spin dynamics of trimer chain with magnetic field. Supplementary Fig. 11 presents the $\mathcal{S}^{xx}(q, \omega)$ for four phases as g is varied. Within XY-I phase, as illustrated in Supplementary Fig. 11 (a1)-(a5), the spectra are all gapless. A weak g value induces the clear separation of spectra with different energy levels, featuring the presence of doublon, upper quarton and lower quarton as we have discussed in the main text. As g increases, the intermediate-energy and high-energy spectra gradually merge, and eventually forming a continuum with the low-energy continuum. When $g = 1$, the trimer chain becomes the Heisenberg XXX model, a little magnetic field ($H_z = 0.1$) induces

an incommensurate order that results in a tiny shift at the lower boundary of two-spinon continuum. In the 1/3 magnetization plateau phase, the gap at $q = \pi$ diminishes with increasing g . The low-energy reduced spin wave, intermediate-energy doublons and high-energy quartons gradually lose their identity and amalgamate as g approaches to 1. Gapless excitations and spectra merging are also observed in the XY-II phase, but there are some distinctions compared to the XY-I phase. For example, when $g = 0.2$, a new energy band emerges near $\omega = 1$ that has no trail in other three phases. For the ferromagnetic phase, the gap at $q = \pi$ decreases as g increases. The excitation spectra are still described by the spin waves, just have two energies for the same wave vector at the Brillouin zone edges due to the periodic potential of the trimerized interaction. When $g = 1$, the system restores the translational invariant symmetry, its excitation spectrum becomes a single one described by a cosine function of momentum.

Supplementary Note 5: Exact diagonalization results

In addition to the DMRG-TDVP and CPT calculations, we have also applied the exact diagonalization (ED) method to study the spin dynamics. The ED method is a fundamental and straightforward approach

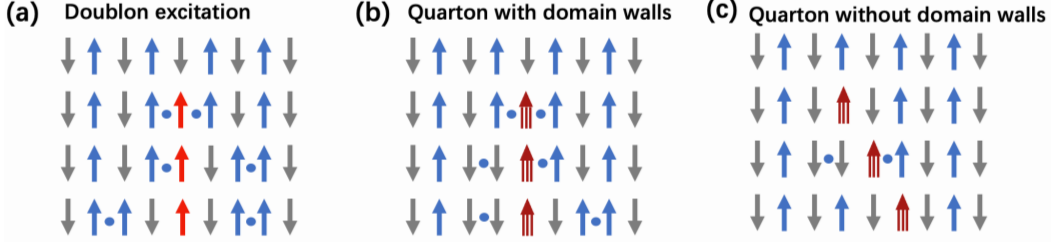


FIG. 9. **Schematic representation of propagating doublon and quarton.** The excitation mechanism and propagation of a quasiparticle are illustrated from top to bottom. Each arrow represents an effective spin of one trimer. (a) A doublon excitation, in which the spinons (domain walls indicated by dots) are bound to one excited trimer indicated by the red color. (b)(c) Quartons with and without domain walls for $\Delta M = 1$. The dark red arrow represents the second excited state of single trimer with $S^z = 3/2$.

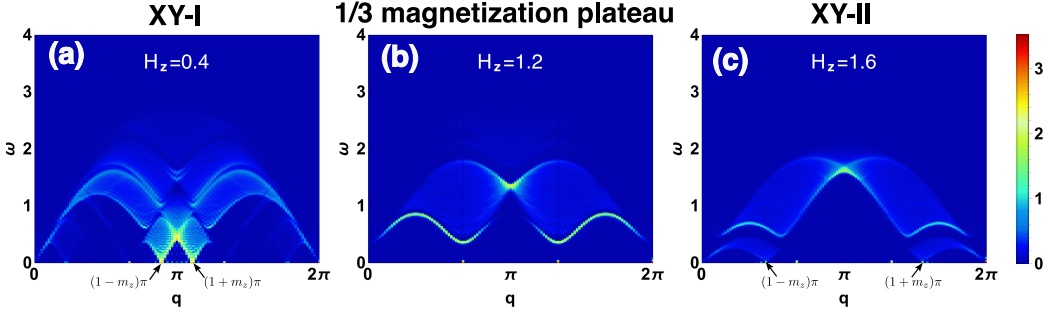


FIG. 10. **Dynamic spin structure factor $\mathcal{S}^{zz}(q, \omega)$ obtained from DMRG-TDVP calculations for different phases.** $\mathcal{S}^{zz}(q, \omega)$ in (a) XY-I phase, (b) 1/3 magnetization plateau phase, and (c) XY-II phase. All results are from the case where $g = 0.8$ and $L = 120$. The color coding of $\mathcal{S}^{zz}(q, \omega)$ uses a piecewise function with the boundary value $U_0 = 2$. Below the boundary, the low-intensity portion is characterized by a linear mapping of the spectral function to the color bar, while above the boundary a logarithmic scale is used, $U = U_0 + \log_{10}[\mathcal{S}^{zz}(q, \omega)] - \log_{10}(U_0)$.

for calculating the eigenenergies and eigenstates for a spin models with small size, which plays a crucial role in analyzing the quantum phase transitions and magnetic excitations in spin systems. In the main text, the quantum critical points of Fig.2(b) and all results in Fig.(4) are obtained through the ED calculations. Initially, we perform ED calculations to obtain reliable results for further investigation, as these calculations are computationally efficient and require minimal resources. When working with larger system sizes, we employ symmetries to block diagonalize the Hamiltonian and reduce computational time and memory usage. Nevertheless, the finite-size effects remain significant. To acquire more dependable insights regarding the thermodynamic limit, advanced numerical methods, such as quantum Monte Carlo, DMRG and CPT are employed. By comparing the results obtained from different methods, we can establish more credible conclusions.

In Supplementary Fig. 12, the longitudinal spin excitations $\mathcal{S}^{zz}(q, \omega)$ of the XY-I, 1/3 magnetization plateau, and XY-II phases are present, which in excellent agreement with the findings presented in Supplementary Fig.10, especially concerning the incommensurate wave numbers at zero energy and the characteristics of excita-

tions spectra of three phases. Furthermore, Supplementary Fig. 13 and Fig. 14 display the results of $\mathcal{S}^{xx}(q, \omega)$ for different phases, which are consistent with the results presented in Figs.(2) and (3) of the main text, respectively.

Supplementary Note 6: Dispersion relations

In the main text, the dispersion relations provide valuable insights into understanding the excitation mechanisms of diverse spin dynamics. When g is small, the intermediate-energy and high-energy excitations are predominantly localized in the trimers. To confirm the nature of these quasiparticles in different phases, we propose a scheme to obtain their dispersion relations based on the imitation of complex ground states. These dispersion relations are consistent with the DMRG-TDVP and CPT results on the location and band widths of excitations spectra (see Fig.3(e) and Fig.5 of main text), indicating that our understanding of the excitation remains accurate, despite the utilization of a highly simplified approximation for the ground state in our calculations.

Here, we outline the main procedures for deriving the dispersion relations. Without magnetic field, the trimer chain can be described by an effective antiferromagnetic

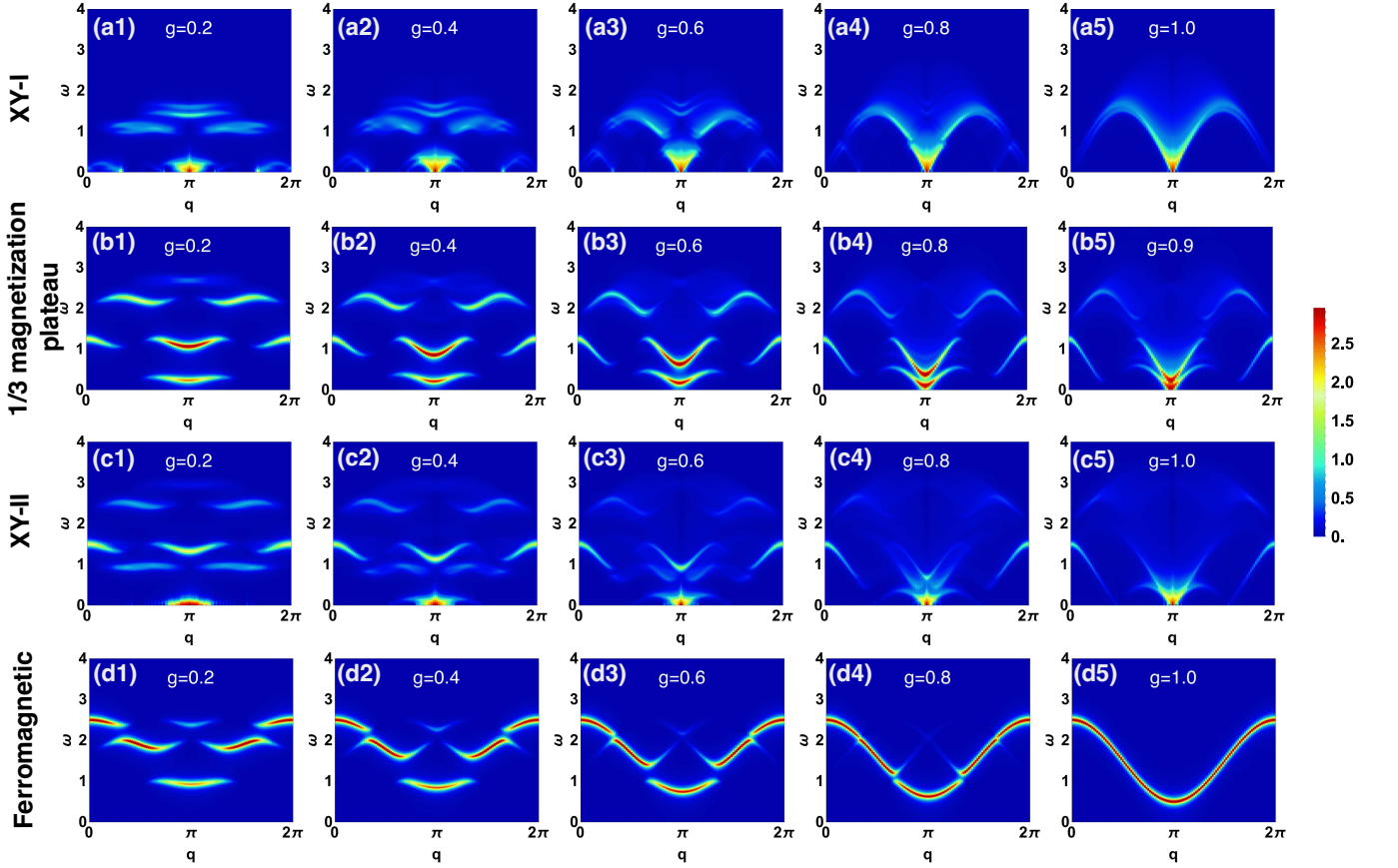


FIG. 11. $S^{xx}(q, \omega)$ obtained from DMRG-TDVP calculations for different phases. $S^{xx}(q, \omega)$ in (a1)-(a5) XY-I phase ($H_z = 0.1$), (b1)-(b5) 1/3 magnetization plateau phase ($H_z = 1.25$), (c1)-(c5) XY-II phase, and (d1)-(d5) ferromagnetic phase ($H_z = 2.0$) for different intertrimer interaction g . All results are from the case where $L = 120$. Particularly, we choose $g = 0.9$ in (b5) for the reason that $H_z = 1.25, g = 1.0$ is a critical point. The color coding of $S^{xx}(q, \omega)$ uses a piecewise function with the boundary value $U_0 = 2$.

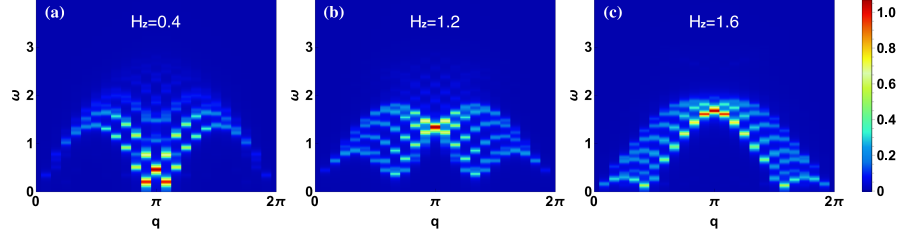


FIG. 12. $S^{zz}(q, \omega)$ obtained from ED calculations for different phases. $S^{zz}(q, \omega)$ in (a) XY-I phase, (b) 1/3 magnetization plateau phase, and (c) XY-II phase. All results are from the case where $g = 0.8$ and $L = 24$. The color coding of $S^{zz}(q, \omega)$ uses a piecewise function with the boundary value $U_0 = 0.2$.

Heisenberg model with the effective interaction dependent on the intertrimer interaction $J_{\text{eff}} = 4J_2/9$ [11]. Due to the weak intertrimer interaction and doubly degenerate ground state, each trimer can be mapped onto an effective spin $S = 1/2$. Therefore, the assumption of the ground-state wave function of spin chain being a product state of ground states of each trimer provides an effective way to simulate the internal trimer excitations. When a

magnetic field is introduced, as discussed in the main text, the quantum phase transition presents, resulting in gapless or gapped ground states in different phases. We have found that the assumption is still valid for analyzing the excitations in the XY-I and 1/3 magnetization plateau phases. In the XY-I phase, we assume that the ground-state wave function of trimer chain is a product

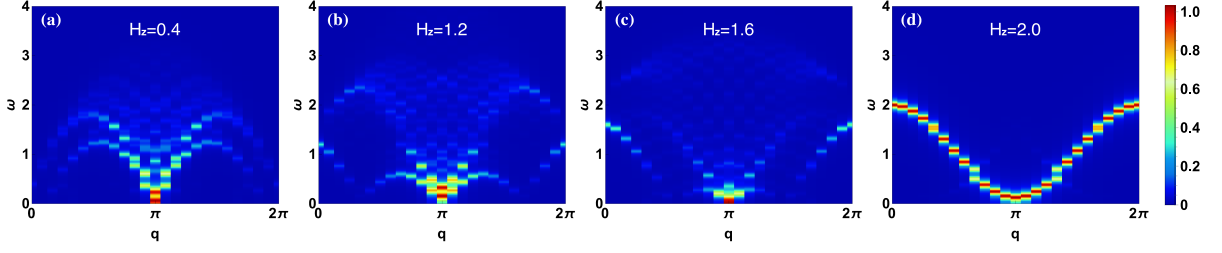


FIG. 13. $S^{xx}(q, \omega)$ obtained from ED calculations for different phases. $S^{xx}(q, \omega)$ in (a) XY-I phase, (b) 1/3 magnetization plateau phase, (c) XY-II phase, and (d) Ferromagnetic phase. All results are from the case where $g = 0.8$ and $L = 24$. The color coding of $S^{xx}(q, \omega)$ uses a piecewise function with the boundary value $U_0 = 0.2$.

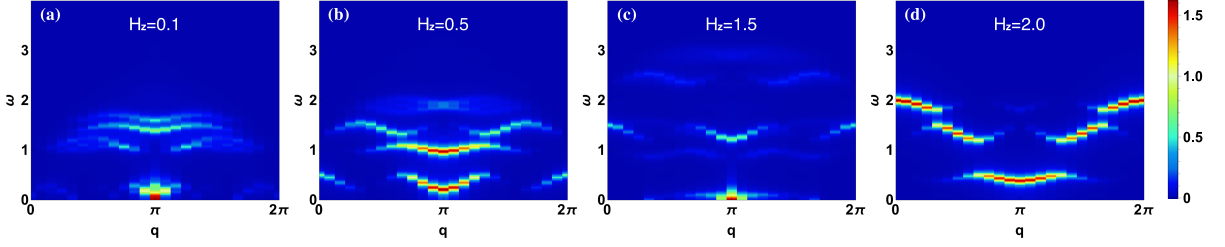


FIG. 14. $S^{xx}(q, \omega)$ obtained from CPT and DMRG-TDVP calculations for different phases with weak inter-trimer interaction. $S^{xx}(q, \omega)$ in (a) XY-I phase, (b) 1/3 magnetization plateau phase, (c) XY-II phase, and (d) Ferromagnetic phase. All results are from the case where $g = 0.3$ and $L = 24$. The color coding of $S^{xx}(q, \omega)$ uses a piecewise function with the boundary value $U_0 = 0.2$.

state of $|0\rangle$ and $|1\rangle$,

$$|\psi\rangle_g = |0\rangle_1 |1\rangle_2 \cdots |0\rangle_{N-1} |1\rangle_N, \quad (29)$$

where $|0\rangle$ and $|1\rangle$ is the ground state and first excited state of a single trimer, as shown in Fig.(4) of main text. We neglect the interactions, and instead deal with 2^{N-1} degenerate ground states, while enforcing the magnetic quantum numbers $\sum M_i = 0$. Even if the magnetic field leads to an incommensurate ground state with a little magnetization, above roughly presupposition still works. It should be noted that we are targeting excitations above the 2^N -fold degenerate ground-state manifold, rather than employing degenerate perturbation theory. In our study, we do not undertake a formal perturbation expansion. Instead, we choose to construct intuitive variational states that encompass the internal excitations of a single trimer.

For the intermediate-energy excitations, we choose the r th trimer to be excited from $|0\rangle$ to $|3\rangle$ with $\Delta M = -1$ or from $|1\rangle$ to $|2\rangle$ with $\Delta M = 1$, the excited wave function is then given by

$$|\psi\rangle_e^r = |0\rangle_1 |1\rangle_2 \cdots |3\rangle_r \cdots |0\rangle_{N-1} |1\rangle_N. \quad (30)$$

To give this excitation a momentum, we perform a Fourier transformation on this excited state, resulting in

$$|\psi\rangle_e^q = \frac{1}{\sqrt{N}} \sum_{r=1}^N e^{-iqr} |\psi\rangle_e^r. \quad (31)$$

Next, we can calculate the expectation values of the Hamiltonian in the ground state and the first excited trimer momentum state to obtain the dispersion relations corresponding to the intermediate-energy excitations in the reduced Hilbert space,

$$\begin{aligned} \epsilon(q) &= \langle H \rangle_e - \langle H \rangle_g \\ &= {}_e^q \langle \psi | H | \psi \rangle_e^q - {}_g^{-q} \langle \psi | H | \psi \rangle_g^{-q}. \end{aligned} \quad (32)$$

Thus, the dispersion relations corresponding to the intermediate-energy doublon are given by,

$$\epsilon_D^{\text{red}}(q) = \begin{cases} -\frac{1}{3}g \cos q + E_1 - E_0 + H_z - \frac{1}{9}g, \\ -\frac{2}{9}g \cos q + E_1 - E_0 + H_z, \\ -\frac{2}{9}g \cos q + E_1 - E_0 + H_z + \frac{2}{9}g, \\ -\frac{2}{9}g \cos q + E_1 - E_0 + H_z + \frac{2}{9}g, \end{cases} \quad (33)$$

which are independent of the length of the spin chain. By replacing q with $3q$, we can obtain the unfolded dispersion relations in full Brillouin zone, as shown in Eq.(11) of main text. To visualize the calculation process, we plot Supplementary Fig. 15, where it can be observed that only 4 trimers are sufficient to obtain all the dispersion relations. For the high-energy excitations, the r -th trimer is excited from $|0\rangle$ to $|4\rangle$ with $\Delta M = 1$ or from $|0\rangle$ to $|6\rangle$ with $\Delta M = -1$. Similar calculations can be

performed to obtain the dispersion relations of the high-energy modes. However, the magnetic field splits the high-energy spectra into two branches due to the diverse spin quantum numbers $\Delta M = \pm 1$. These branches are referred to as the upper quarton and lower quarton (see Eq.(12) and Eq.(13) of main text), respectively.

In the $1/3$ magnetization plateau phase, the gapped ground state simplifies the calculations. As depicted in Supplementary Fig. 15(b), the ground state is constructed from product of polarized trimers (as the effective spins $S_{\text{eff}} = 1/2$). The low-energy excitation originates from a flipped effective spin, similar to the formation of spin wave, but in a reduced Hilbert space. Therefore, the excitation from $|0\rangle$ to $|1\rangle$ with $\Delta M = -1$ is described by the reduced spin wave.

Other excitations also arise from the internal trimer excitations, such as $|0\rangle \rightarrow |3\rangle$ with $\Delta M = -1$, $|0\rangle \rightarrow |4\rangle$ with $\Delta M = 1$, and $|0\rangle \rightarrow |6\rangle$ with $\Delta M = -1$. Each excitation has only one dispersion relation which consists well with the excitation spectrum. At the high-energy regime, the presence of a continuum with weak weight may originate from the fractional spinons, as discussed in our previous study [11]. Furthermore, in Supplementary Fig. 16, we show that the gap between ground state and first excited state provides effective protection for the excitations mentioned above. Even when the intertrimer interaction increases to $g = 0.8$, the dispersion relations still effectively capture the internal trimer excitations. A higher value of the intertrimer interaction g leads to the merging of these excitation spectra and gives rise to the formation of a continuum.

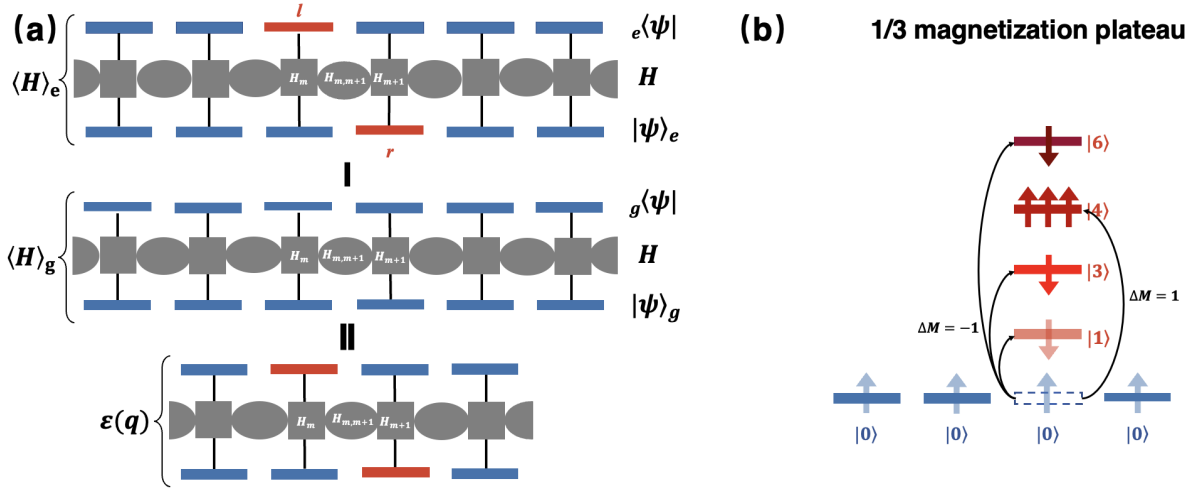


FIG. 15. **Graphical representation of the calculation of the dispersion relation $\epsilon(q) = \langle H \rangle_e - \langle H \rangle_g$.** (a) The trimer eigenstates are shown as darker blue (ground states) and red (excited states). With these states, the excitations with $|\Delta M| = 1$ originate from a trimer ground state $|0\rangle_r^1$ on the trimer located at r when excited to one of $|1\rangle_r$, $|3\rangle_r$, $|4\rangle_r$, and $|6\rangle_r$ (and in the corresponding bra states we use the site index l instead of r). The excitations are given momentum q , and the matrix elements contributing to the dispersion relation are indicated. (b) The construction of ground state and excitation mechanism in the 1/3 magnetization plateau phase.

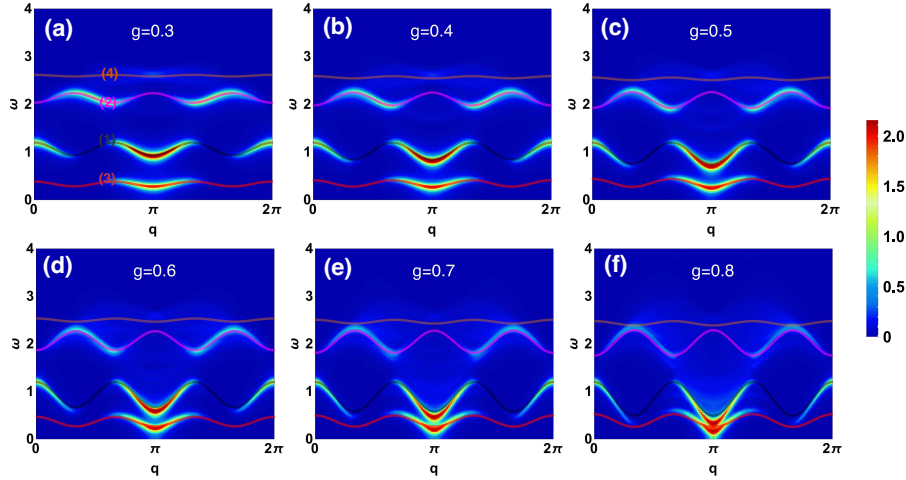


FIG. 16. $S^{xx}(q, \omega)$ in 1/3 magnetization plateau phase for different g . All results are obtained by DMRG-TDVP calculations for $L = 120$, $H_z = 1.2$, and the color coding of $S^{xx}(q, \omega)$ uses a piecewise function with the boundary value $U_0 = 2$. The dispersion lines with colors and numbers are corresponding to the different localized excitations in a single trimer. (1)(2)(4) are the excitations from $|0\rangle \rightarrow |1\rangle$, $|0\rangle \rightarrow |3\rangle$ and $|0\rangle \rightarrow |6\rangle$ with $\Delta M = -1$, respectively. (3) is the excitations from $|0\rangle \rightarrow |4\rangle$ with $\Delta M = 1$.